Production mechanism of proton-rich actinide isotopes in fusion reactions and via multinucleon transfer processes

Peng-Hui Chen,[1,2,3] Fei Niu,[1] and Zhao-Qing Feng[1,*]

[1]*School of Physics and Optoelectronics, South China University of Technology, Guangzhou 510640, China*
[2]*Institute of Modern Physics, Chinese Academy of Sciences, Lanzhou 730000, China*
[3]*School of Nuclear Science and Technology, University of Chinese Academy of Sciences, Beijing 100190, China*

(Received 23 April 2020; accepted 13 July 2020; published 30 July 2020)

Within the framework of the dinuclear system model, the reaction mechanism for producing the proton-rich actinide isotopes $Z = 93$–100 near the proton drip line is thoroughly investigated in the fusion reactions with ^{24}Mg, ^{28}Si, ^{32}S, ^{36,40}Ar, and ^{40}Ca bombarding the target nuclei ^{181}Ta, ^{180}W, ^{185}Re, ^{184}Os, ^{191}Ir, ^{190}Pt, ^{197}Au, ^{196}Hg, ^{203}Tl, ^{204}Pb, and ^{209}Bi, and in the multinucleon transfer reactions with proton-rich radioactive beams ^{59}Cu, ^{69}As, ^{90}Nb, ^{91}Tc, ^{94}Rh, ^{105,110}Sn, and ^{118}Xe on ^{238}U near Coulomb barrier energies. The production cross sections of new proton-rich isotopes in the fusion-evaporation reactions and fragment yields in the multinucleon transfer reactions are estimated systematically and compared in both reaction mechanisms, in which a statistical approach is used to describe the decay process of excited nuclei. A dynamical deformation is implemented in the model in the dissipation process. It is found that charged particle evaporation channels (alpha and proton) dominate in the decay process of proton-rich nuclides. The fusion-evaporation reactions are favorable to produce the new neutron-deficient actinide isotopes. The total kinetic energies and angular spectra of primary fragments in multinucleon transfer reactions are strongly dependent on colliding orientations and incident energies.

DOI: 10.1103/PhysRevC.102.014621

I. INTRODUCTION

In the past decades, studies on producing neutron-deficient actinide nuclei have been performed continually at the Institute of Modern Physics (IMP, Lanzhou), Flerov Laboratory of Nuclear Reactions (FLNR, Dubna), and Lawrence Berkeley National Laboratory (LBNL, Berkeley). The new proton-rich isotopes were synthesized in experiments through fusion-evaporation reactions by detecting the alpha decay chains [1–4]. The products in the fusion-evaporation (FE) reactions are closely associated with the projectile-target mass asymmetry and the structure of the reaction system. Normally, the combination of a light projectile nucleus with a heavy target is used for creating the proton-rich actinide isotopes through a fusion-evaporation reaction, for instance, $^{36}\mathrm{Ar} + {}^{208}\mathrm{Pb} \rightarrow {}^{244}\mathrm{Fm}$, $^{40}\mathrm{Ca} + {}^{196}\mathrm{Hg} \rightarrow {}^{236}\mathrm{Fm}$, etc. On the other hand, the multinucleon transfer (MNT) reactions based on neutron-deficient beams might be a possible way. In the experiment for synthesizing superheavy nuclei (SHN) with $^{48}\mathrm{Ca} + {}^{248}\mathrm{Cm}$ [5], five new neutron-deficient isotopes, ^{216}U, ^{219}Np, ^{223}Am, ^{229}Am, and ^{233}Bk, have been identified, in which the MNT process dominates the new isotope formation. This has the advantage that the products are formed in a broad mass regime for the MNT products. The neutron-deficient radioactive beams such as ^{105,110,115}Sn ^{58}Cu, ^{69}As, ^{90}Nb, ^{94}Rh, and ^{118}Xe can be generated in radioactive beam facilities, for instance, the Beijing Rare Ion beam Facility (BRIF), the Beijing Isotope-Separation On Line (BISOL) facility, and the Radioactive Ion Beam Facility (BIBM, RIKEN) [6]. The MNT reaction within neutron-deficient beams might be favorable to approach the neutron-deficient actinide region due to isospin relaxation. On the other hand, the properties of neutron-deficient heavy isotopes are crucial for exploring the proton drip line and shell evolution. The MNT reactions, instead of fusion-evaporation reactions, might be a possible way to produce neutron-deficient heavy isotopes in the nuclide chart.

Following the motivation for producing heavy new isotopes, several models have been developed for describing the transfer reactions, i.e., the dynamical model based on multidimensional Langevin equations [7,8], the time-dependent Hartree-Fock (TDHF) approach [9–12], the GRAZING model [13,14], the improved quantum molecular dynamics (ImQMD) model [15], the dinuclear system (DNS) model [16,17], etc. Some interesting issues have been stressed, e.g., the production cross sections of new isotopes, total kinetic energy spectra of transfer fragments, structure effect on the fragment formation, and angle distributions of MNT products. There are still some open problems for the transfer reactions, i.e., including the mechanism of preequilibrium cluster emission, the stiffness of nuclear surface during the nucleon transfer process, the mass limit of new isotopes with stable heavy target nuclides, etc. Traditionally, neutron-deficient heavy nuclei have been produced through the fusion-evaporation mechanism, which has a shortcoming for producing extreme neutron-deficient actinide nuclei due to small fusion probability. The MNT reactions might provide a possible way to approach creating neutron-deficient actinide isotopes close to the proton drip line.

*Corresponding author: fengzhq@scut.edu.cn

The transfer reactions and deep inelastic heavy-ion collisions have benn extensively investigated in experiments since 1970s, in which the new neutron-rich isotopes of light nuclei and pronton-rich actinide nuclei were observed [18–24]. The reaction mechanism and fragment formation were investigated thoroughly, i.e., the energy and angular momentum dissipation, two-body kinematics, shell effect, fission of actinide nuclei, etc. Recently, more measurements have been performed at different laboratories for creating the neutron-rich heavy nuclei, e.g., the reactions of ^{136}Xe + ^{208}Pb [25,26], ^{136}Xe + ^{198}Pt [27], ^{156,160}Gd + ^{186}W [28], and ^{238}U + ^{232}Th [29]. The MNT reactions with radioactive beams are feasible for producing new isotopes owing to the large mass drift and isospin diffusion [30,31].

In this work, the ^{40}Ca, ^{36}Ar, ^{32}S, ^{28}Si, and ^{24}Mg induced fusion-evaporation reactions and the MNT reactions with the combinations of ^{105,110,115,120,125,130}Sn ^{58}Cu, ^{69}As, ^{90}Nb, ^{94}Rh, and ^{118}Xe with ^{238}U are calculated with the DNS model. The article is organized as follows: In Sec. II we give a brief description of the DNS model. Calculated results and discussion are presented in Sec. III. A summary is given in Sec. IV.

II. MODEL DESCRIPTION

The DNS concept was proposed by Volkov for describing deep inelastic heavy-ion collisions [32], in which few-nucleon transfer was treated. Application of the approach to superheavy nucleus formation via massive fusion reactions in competition with the quasifission process was used for the first time by Adamian *et al.* [33,34]. The modifications of the relative motion energy and angular momentum of two colliding nuclei coupling to nucleon transfer within the DNS concept were performed by the Lanzhou Group [35–37]. The production cross sections of SHN, quasifission, and fusion-fission dynamics have been extensively investigated within the DNS model [38,39]. The dynamical evolution of a colliding system sequentially proceeds through the capture process by overcoming the Coulomb barrier to form the DNS; the relaxation process of the relative motion energy, angular momentum, mass, and charge asymmetry, etc., within the potential energy surface; and the deexcitation of primary fragments.

The distribution probability is obtained by solving a set of master equations numerically in the potential energy surface of the DNS. The time evolution of the distribution probability $P(Z_1, N_1, E_1, \beta, t)$ for fragment 1 with proton number Z_1, neutron number N_1, excitation energy E_1, and quadrupole deformation β is described by the following master equations:

$$\begin{aligned}\frac{dP(Z_1,N_1,E_1,\beta,t)}{dt} &= \sum_{Z_1'} W_{Z_1,N_1,\beta;Z_1',N_1,\beta}(t)[d_{Z_1,N_1}P(Z_1',N_1,E_1',\beta,t) \\ &\quad - d_{Z_1',N_1}P(Z_1,N_1,E_1,\beta,t)] \\ &\quad + \sum_{N_1'} W_{Z_1,N_1,\beta;Z_1,N_1',\beta}(t)[d_{Z_1,N_1}P(Z_1,N_1',E_1',\beta,t) \\ &\quad - d_{Z_1,N_1'}P(Z_1,N_1,E_1,\beta,t)] \end{aligned} \quad (1)$$

Here the $W_{Z_1,N_1,\beta;Z_1',N_1,\beta}(W_{Z_1,N_1,\beta,;Z_1,N_1',\beta})$ is the mean transition probability from the channel (Z_1, N_1, E_1, β) to (Z_1', N_1, E_1', β), [or (Z_1, N_1, E_1, β) to (Z_1, N_1', E_1', β)], and d_{Z_1,Z_1} denotes the microscopic dimension corresponding to the macroscopic state (Z_1, N_1, E_1).The sum is taken over all possible proton and neutron numbers that fragment Z_1', N_1' may take, but only one nucleon transfer is considered in the model with the relations $Z_1' = Z_1 \pm 1$ and $N_1' = N_1 \pm 1$. The dynamical evolution of quadrupole deformation is expressed by $\beta = \beta_P'(t)$ for projectilelike fragments and $\beta = \beta_T'(t)$ for targetlike fragments. It is noticed that the decay of DNS is not taken into account because of the vanishing quasifission barrier, which was included in the fusion-evaporation reactions. Actually, the decay of the DNS has been effectively considered by shortening the interaction time for describing the MNT reactions.

The motion of nucleons in the interacting potential is governed by the single-particle Hamiltonian. The excited DNS opens a valence space in which the valence nucleons have a symmetrical distribution around the Fermi surface. Only the particles at the states within the valence space are active for nucleon transfer. The transition probability is related to the local excitation energy and nucleon transfer, which is microscopically derived from the interaction potential in valence space as

$$W_{Z_1,N_1;Z_1',N_1} = \frac{\tau_{\rm mem}(Z_1,N_1,E_1;Z_1',N_1,E_1')}{d_{Z_1,N_1}d_{Z_1',N_1}\hbar^2} \times \sum_{ii'} |\langle Z_1',N_1,E_1',i'|V|Z_1,N_1,E_1,i\rangle|^2. \quad (2)$$

The transition coefficients determine the distribution width of the isotopic yields in the MNT reactions. The memory time $\tau_{\rm mem}$ is extracted from the deep inelastic heavy-ion collisions and associated with the angular momentum of colliding partners [40]. The matrix element V of the interaction potential is assumed from the nucleon transfer between two Fermi surfaces of DNS fragments formed in the touching configuration [41].

The averages on these quantities are performed in the valence space as follows:

$$\Delta\varepsilon_K = \sqrt{\frac{4\varepsilon_K^*}{g_K}}, \quad \varepsilon_K^* = \varepsilon^*\frac{A_K}{A}, \quad g_K = A_K/12, \quad (3)$$

where the ε^* is the local excitation energy of the DNS. The microscopic dimension for the fragment (Z_K, N_K) is evaluated by the valence states $N_K = g_K\Delta\varepsilon_K$ and the valence nucleons $m_K = N_K/2$ $(K = 1, 2)$ as

$$d(m_1, m_2) = \binom{N_1}{m_1}\binom{N_2}{m_2}. \quad (4)$$

In the relaxation process of the relative motion, the DNS will be excited by the dissipation of the relative kinetic energy. The local excitation energy is determined by the dissipation energy from the relative motion and the potential energy surface of the DNS as

$$\varepsilon^*(t) = E^{\rm diss}(t) - [U(\{\alpha\}) - U(\{\alpha_{EN}\})]. \quad (5)$$

The entrance channel quantities $\{\alpha_{EN}\}$ include the proton and neutron numbers, quadrupole deformation parameters, and orientation angles, which are

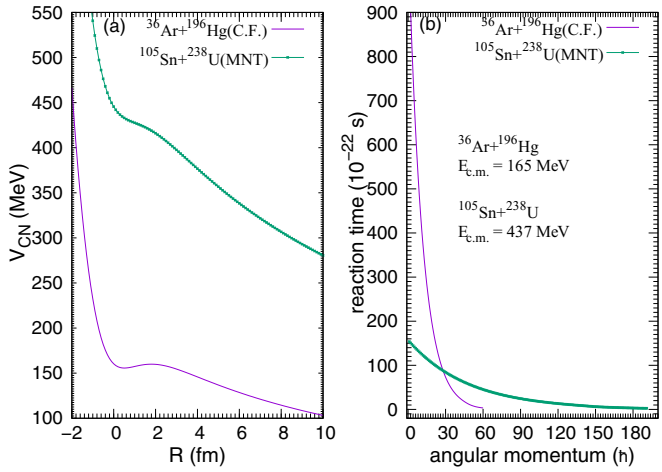

FIG. 1. (a) The interaction potentials and (b) angular momentum dependence of the reaction time in the fusion-evaporation reaction $^{36}\mathrm{Ar}+{}^{196}\mathrm{Hg}$ and in the MNT reaction $^{105}\mathrm{Sn}+{}^{238}\mathrm{U}$.

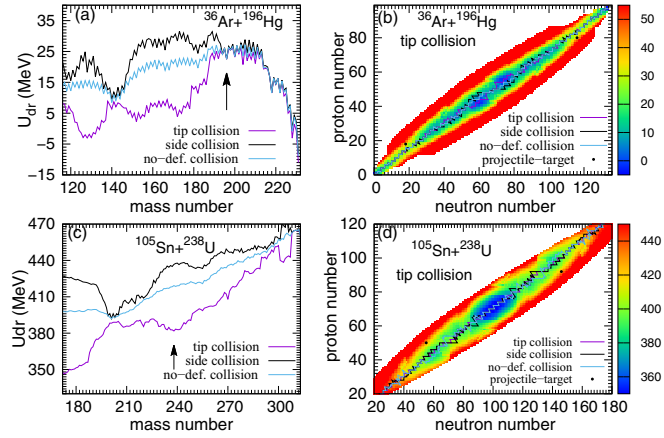

FIG. 2. Potential energy surfaces of $^{36}\mathrm{Ar}+{}^{196}\mathrm{Hg}$ and $^{105}\mathrm{Sn}+{}^{238}\mathrm{U}$ with the tip-tip, side-side, and no-deformation collisions. The entrance channels are marked by arrows and black solid circles.

Z_P, N_P, Z_T, N_T, R, β_P, β_T, θ_P, θ_T for projectile and target nuclei with the symbols of P and T, respectively. The excitation energy E_1 for fragment (Z_1, N_1) is evaluated by $E_1 = \varepsilon^*(t = \tau_{\rm int})A_1/A$.

The interaction time $\tau_{\rm int}$ is obtained from the deflection function method [42]. The interaction potential is composed of Coulomb and nuclear potentials which are calculated by the Wong formula and the double folding formalism [43]. The interaction potential energy distribution and interaction time for the systems of $^{36}\mathrm{Ar}+{}^{196}\mathrm{Hg}$ (magenta line) and $^{105}\mathrm{Sn}+{}^{238}\mathrm{U}$ (green dotted line) reactions are shown in Fig. 1. It should be noticed that there is no potential pocket for the heavy systems. The interaction decreases exponentially with increasing angular momentum. The existence of the pocket in the entrance channel is crucial for the compound nucleus formation in fusion reactions [44]. The barrier is taken as the potential value at the touching configuration and the nucleus-nucleus potential is calculated with the same approach as in fusion reactions [37]. According to Fig. 1, we found that light systems have a longer interaction time due to the potential pocket (Coulomb barrier), in comparison with heavy systems. The lifetime of the DNS is strongly reduced in the MNT reactions in comparison to the fusion-evaporation reactions, i.e., the half-width value of relaxation time is 50×10^{-22} s for the system $^{105}\mathrm{Sn}+{}^{238}\mathrm{U}$ and 300×10^{-22} s for the reaction $^{36}\mathrm{Ar}+{}^{196}\mathrm{Hg}$.

The energy dissipated into the DNS is expressed as

$$E^{\rm diss}(t) = E_{c.m.} - B - \frac{\langle J(t)\rangle[\langle J(t)\rangle + 1]\hbar^2}{2\zeta} - \langle E_{\rm rad}(J,t)\rangle. \quad (6)$$

Here the $E_{c.m.}$ and B are the center-of-mass energy and Coulomb barrier, respectively. The radial energy is evaluated from

$$\langle E_{\rm rad}(J,t)\rangle = E_{\rm rad}(J,0)\exp(-t/\tau_r). \quad (7)$$

The relaxation time of the radial motion is $\tau_r = 5 \times 10^{-22}$ s and the radial energy at the initial state is $E_{\rm rad}(J,0) = E_{c.m.} - B - J_i(J_i+1)\hbar^2/(2\zeta_{\rm rel})$. The dissipation of the relative angular momentum is described by

$$\langle J(t)\rangle = J_{st} + (J_i - J_{st})\exp(-t/\tau_J). \quad (8)$$

The angular momentum at the sticking limit is $J_{st} = J_i\zeta_{\rm rel}/\zeta_{\rm tot}$ and the relaxation time is $\tau_J = 15 \times 10^{-22}$ s. The $\zeta_{\rm rel}$ and $\zeta_{\rm tot}$ are the relative and total moments of inertia of the DNS, respectively, in which the quadrupole deformations are implemented [45]. The initial angular momentum is set to be $J_i = J$ in the following work. In the relaxation process of the relative motion, the DNS will be excited by the dissipation of the relative kinetic energy.

The local excitation energy is determined by the excitation energy of the composite system and the potential energy surface (PES) of the DNS. The PES is evaluated by

$$U_{dr}(t) = Q_{gg} + V_C(Z_1, N_1, \beta_1, Z_2, N_2, \beta_2, t) + V_N(Z_1, N_1, \beta_1, Z_2, N_2, \beta_2, t) + V_{\rm def}(t) \quad (9)$$

with

$$V_{\rm def}(t) = \frac{1}{2}C_1[\beta_1 - \beta_T'(t)]^2 + \frac{1}{2}C_2[\beta_2 - \beta_P'(t)]^2, \quad (10)$$

$$C_i = (\lambda-1)(\lambda+2)R_i^2\delta - \frac{3}{2\pi}\frac{Z_i^2}{R_i(2\lambda+1)}, \quad (11)$$

which satisfies the relation of $Z_1 + Z_2 = Z$ and $N_1 + N_2 = N$, with the Z and N being the proton and neutron numbers of the composite system, respectively. Here, we only take into account the quadrupole deformation ($\lambda = 2$). The σ is the coefficient of surface tension which satisfies $4\pi R_i^2\sigma = a_s A_i^{2/3}$ with the surface energy $a_s = 18.32$ MeV and the nuclear radius R_i. The symbol α denotes the quantities of Z_1, N_1, Z_2, N_2, J, R, β_1, β_2, θ_1, θ_2. The $B(Z_i, N_i)$ $(i = 1, 2)$ and $B(Z, N)$ are the negative binding energies of the fragment (Z_i, N_i) and the composite system (Z, N), respectively. The θ_i denotes the angles between the collision orientations and the symmetry axes of the deformed nuclei. Shown in Fig. 2

are the PESs in the tip-tip collisions of $^{105}\mathrm{Sn}+^{238}\mathrm{U}$ and $^{36}\mathrm{Ar}+^{196}\mathrm{Hg}$. The DNS fragments towards the mass symmetric valley release positive energy, which is available for nucleon transfer. The spectra exhibit a symmetric distribution for each isotopic chain. The valley in the PES is close to the β-stability line and enables the diffusion of the fragment probability. The entrance positions of projectile and target nuclei are indicated by black dots in the PES contour graphs. The occupation probability diffuses from the entrance position to possible states after overcoming the local potential energy. The evolutions of quadrupole deformations of projectilelike and targetlike fragments proceed from the initial configuration as

$$\beta'_P(t) = \beta_P \exp(-t/\tau_\beta) + \beta_1[1-\exp(-t/\tau_\beta)],$$
$$\beta'_T(t) = \beta_T \exp(-t/\tau_\beta) + \beta_2[1-\exp(-t/\tau_\beta)] \quad (12)$$

with the deformation relaxation of $\tau_\beta = 40\times10^{-22}$ s. The β_1 and β_2 are the ground-state deformations of DNS fragments and the projectile (target) quadrupole deformation corresponding to β_P (β_T).

The total kinetic energy (TKE) of the primary fragment is evaluated by

$$\mathrm{TKE}(A_1) = E_{c.m.} + Q_{gg}(A_1) - E^{\mathrm{diss}}(t=\tau_{\mathrm{int}}), \quad (13)$$

where $Q_{gg} = M_P + M_T - M_{PLF} - M_{TLF}$ and $E_{c.m.}$ is the incident energy in the center-of-mass frame. The masses M_P, M_T, M_{PLF} and M_{TLF} correspond to projectile, target, projectilelike fragment, and targetlike fragment, respectively. Figure 3 shows the calculated total kinetic energy (TKE) and the mass distributions of the primary products with inclusive mass distribution for the $^{105}\mathrm{Sn}+^{238}\mathrm{U}$ reaction with three types of collision orientations at a near-barrier energy of $E_{\mathrm{lab}} =$ 6 MeV/nucleon. The TKE is highly dependent on the initial orientation of the deformed ^{105}Sn and ^{238}U nuclei, caused by the PES. The formation of DNS fragments tends toward the symmetric pathway (quasifission process). The spectra exhibit a symmetric mass distribution because of the structure in the PES. We found that TKE and mass distributions with the tip-tip collision are wider than those in side-side and no-deformation collisions. The tail of the TKE distribution can reach very low kinetic energy with small yields due to massive kinetic energy dissipation. The large yields of the fragments in the region from the target position to the doubly magic nucleus ^{208}Pb are the most pronounced feature of the TKE distribution.

The cross sections of the survival fragments produced in the MNT reactions and the evaporation residue cross sections are evaluated by

$$\sigma_{MNT}(Z_1,N_1,E_{c.m.}) = \frac{\pi\hbar^2}{2\mu E_{c.m.}}\sum_{J=0}^{J_{\max}}(2J+1) \times \int f(B)T(E_{c.m.},J,B) \times \sum_s P(Z'_1,N'_1,E'_1,J'_1,B) \times W_{sur}(Z'_1,N'_1,E'_1,J'_1,s)dB \quad (14)$$

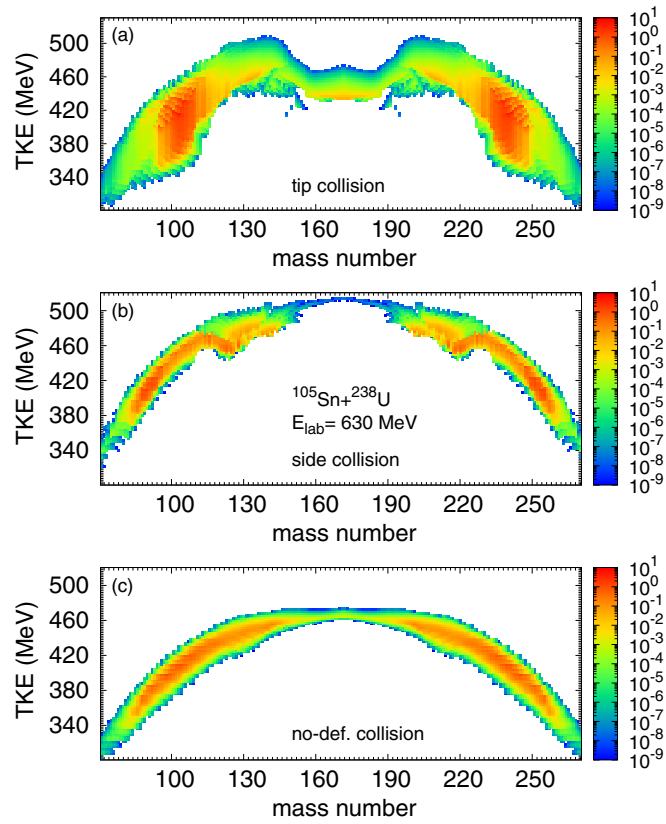

FIG. 3. The total kinetic energy and mass distributions of the primary fragments produced in the MNT reactions of $^{105}\mathrm{Sn}+^{238}\mathrm{U}$ collisions at $E_{\mathrm{lab}} = 6$ MeV/nucleon with the (a) tip-tip, (b) side-side, and (c) no-deformation collisions.

and

$$\sigma^s_{ER}(E_{c.m.}) = \frac{\pi\hbar^2}{2\mu E_{c.m.}}\sum_{J=0}^{J_{max}}(2J+1)T(E_{c.m.},J) \times P_{CN}(E_{c.m.},J)W^s_{sur}(E_{c.m.},J), \quad (15)$$

respectively. The μ is the reduced mass of relative motion in the colliding system. The transmission probability $T(E_{c.m.},J)$ is taken as zero or unity corresponding the incident energy $E_{c.m.}$ in the center-of-mass frame below or above the summation value of the attempted barrier B and the rotational energy at the relative angular momentum J. The E_1 and J_1 are the excitation energy and the angular momentum for the fragment (Z_1,N_1). The maximal angular momentum $J_{\max}$ is taken to be the grazing collision of two nuclei. The survival probability W_{sur} of each fragment is evaluated with a statistical approach based on the Weisskopf evaporation theory [46], in which the excited primary fragments are cooled in evaporation channels $s(Z_s,N_s)$ by γ rays and light particles (neutrons, protons, α's, etc.) in competition with the binary fission via $Z_1 = Z'_1 - Z_s$ and $N_1 = N'_1 - N_s$. The $P_{CN}(E_{c.m.},J)$ are fusion probabilities which sum over all the fragments' probabilities located outside of the BG (Businaro-Gallone) point. The transferred cross section is smoothed with the barrier distribution and the function is taken to have the Gaussian form of $f(B) = \frac{1}{N}\exp[-\{(B-B_m)/\Delta\}^2]$ with the normalization constant

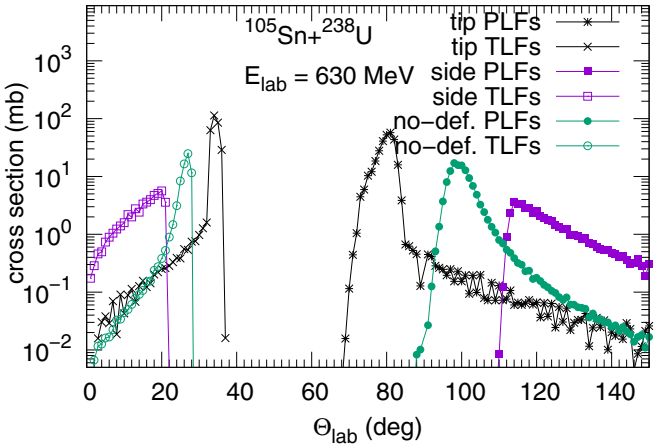

FIG. 4. The angular distributions of the Sn-like and U-like products in the laboratory frame in the MNT reactions of ^{105}Sn + ^{238}U collisions at $E_{lab} = 6$ MeV/nucleon with different collision orientations.

satisfying the unity relation $\int f(B)dB = 1$. The quantities B_m and Δ are evaluated by $B_m = (B_C + B_S)/2$ and $\Delta = (B_C - B_S)/2$, respectively. The B_C and B_S are the Coulomb barrier at waist-to-waist orientation and the minimum barrier by varying the quadrupole deformation parameters of colliding partners.

III. RESULTS AND DISCUSSION

The complete fusion reaction mechanism has been used to synthesize many new heavy and superheavy nuclei experimentally. Recently, due to renewed interest, the damped collisions of two heavy nuclei were investigated and for producing heavy isotopes, in particular new nuclides close to proton- and neutron-rich drip lines. The DNS model can nicely reproduce the production cross sections of fusion-evaporation products and MNT yields [47–53]. The fragment yields in the MNT reactions are related to the emission angle in the laboratory system. It was observed that the clusters formed in the massive transfer reactions were emitted anisotropically [54]. A prediction of the polar angle structure for the MNT fragments is helpful for managing the detector system in experiments. The emission angle of the reaction products is helpful for arranging detectors in experiments. We use a deflection function method to evaluate the fragment angle which is related to the mass of the fragment, angular momentum, and incident energy. The deflection angle is composed of the Coulomb and nuclear interactions [42,52]. Shown in Fig. 4 are the PLF and TLF angular distributions of primary fragments from transferring 20 nucleons in the reaction of ^{105}Sn + ^{238}U at the laboratory incident energy of $E_{lab} =$ 6 MeV/nucleon. The emission of MNT fragments is associated with the collision orientation, i.e., the peak varies from angles of 80° to 110° with the tip-tip to side-side orientation for the PLFs. The PLFs are distributed in a broad polar angle regime in comparison with the TLFs owing to the contribution of low angular momenta.

Shown in Fig. 5 are the cross sections for isotopes $Z =$ 93–100 in the MNT reactions of tin isotope induced ^{238}U

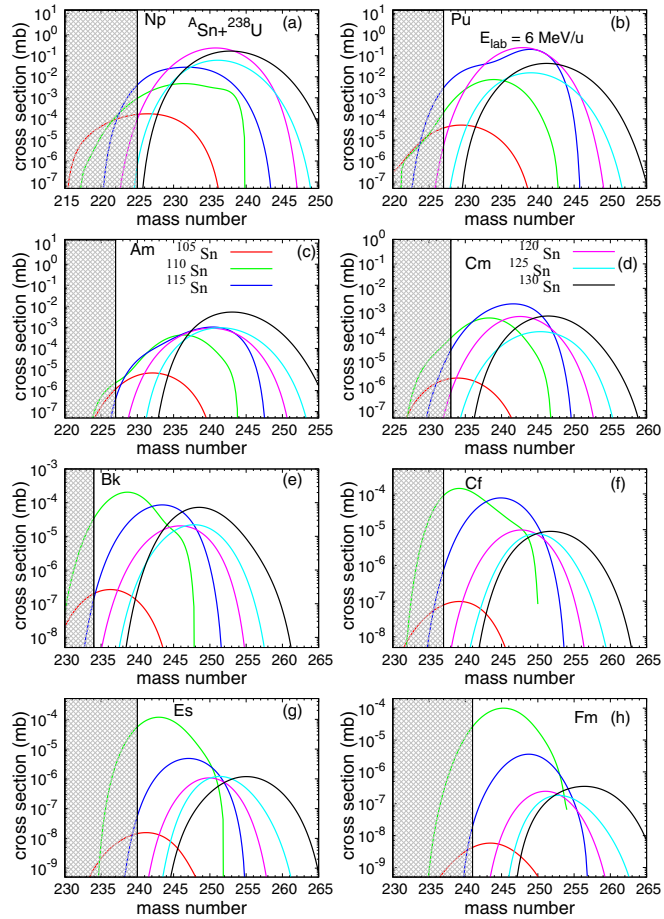

FIG. 5. Cross sections for producing heavy neutron-deficient isotopes from the transfer reactions ^{105}Sn + ^{238}U (red line), ^{110}Sn + ^{238}U (green line), ^{115}Sn + ^{238}U (blue line), ^{120}Sn + ^{238}U (pink line), ^{125}Sn + ^{238}U (cyan line), and ^{130}Sn + ^{238}U (black line) at the incident energy 6 MeV/nucleon. The grid line region indicates unknown isotopes.

collisions at the laboratory energy of $E_{lab} = 6$ MeV/nucleon. The projectile nuclei are ^{105}Sn, ^{110}Sn, ^{115}Sn, ^{120}Sn, ^{125}Sn, and ^{130}Sn. It is interesting to compare the production cross sections for different Sn projectiles bombarding the same target ^{238}U through the MNT reaction. For the colliding systems ^{105,110,115,120,125,130}Sn + ^{238}U, the neptunium (Np), plutonium (Pu), americium (Am), curium (Cm), berkelium (Bk), californium (Cf), einsteinium (Es), and fermium (Fm) neutron-deficient isotopes may be created by transferring one to eight protons from projectile to target nuclei and a few neutron transfers in the inverse process. The calculated production cross sections of neutron-deficient isotopes $Z = 93$–100 increase with decreasing the N/Z ratios of Sn isotopes. The more neutron-poor isotopes are favorable for the new isotope formation in the MNT reactions. The grid region indicates unknown neutron-deficient isotopes as shown in Fig. 5. The reaction system with smaller N/Z ratio enhances the formation of proton-rich actinide nuclides. For example, the reactions induced by ^{115}Sn are favorable for producing unknown neutron-deficient ^{227}Np and ^{233}Pu with

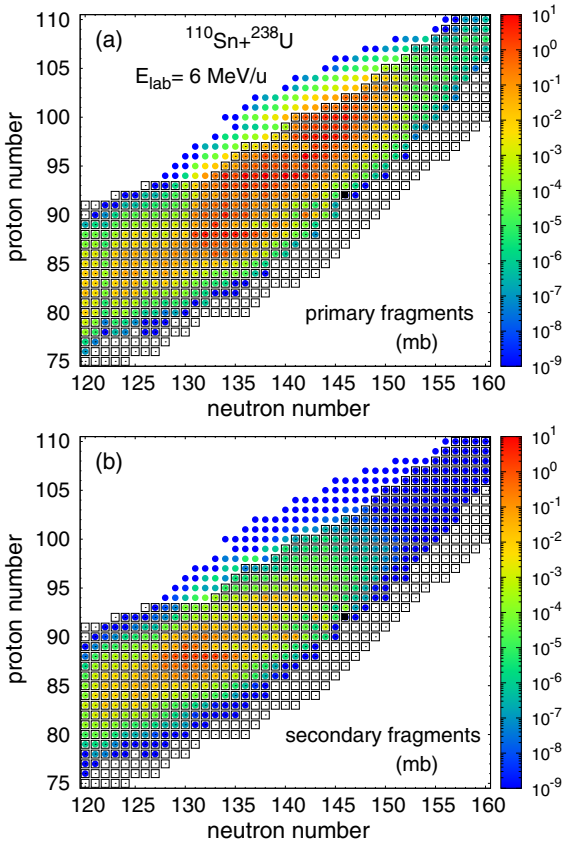

FIG. 6. Contour plot of production cross sections as functions of neutron and proton numbers of primary fragments and secondary fragments in collisions of $^{105}\mathrm{Sn} + ^{238}\mathrm{U}$ at the incident energy $E_{\mathrm{lab}} =$ 6 MeV/nucleon. The open squares and solid circles stand for known isotopes [55] and proton-rich unknown isotopes, respectively.

the cross sections of 10 and 96 μb, respectively, while the bombardment of ^{110}Sn on ^{238}U leads to the production of ^{234}Am, ^{237}Cm, ^{234}Bk, ^{237}Cf, ^{240}Es, and ^{241}Fm with the cross sections of 138 nb, 350 nb, 149 pb, 717 pb, 619 pb, and 167 pb, respectively. The difference of ^{110}Sn and ^{115}Sn induced reactions is caused by the deformation effect.

Neutron-deficient Sn isotopes can be generated by the proton or neutron induced asymmetric fission of actinide nuclide, for instance, at the radioactive beam facilities Beijing Rare Ion Beam Facility (BRIF) and the future Beijing Isotope-Separation on Line (BISOL). The contour plot of primary and secondary fragments ($Z > 75$, $N > 120$) in collisions of $^{110}\mathrm{Sn} + ^{238}\mathrm{U}$ at $E_{\mathrm{lab}} = 6$ MeV/nucleon are calculated as shown in Fig. 6. The open squares and solid circles stand for known isotopes within the mass table [55] and proton-rich unknown isotopes, respectively. The primary fragments are produced on the neutron-deficient side caused by isospin relaxation. The deexcitation process moves the fragments to the β-stability line and even the neutron-rich side through emission of charged particles. The solid color circles outside open squares are predicted unknown neutron-deficient isotopes. It is obvious that the deexcitation process reduces the mass region and a number of proton-rich nuclides might be created via the MNT reactions.

It is of interest to compare the production cross section from different projectile isotopes bombarding the same target through the MNT reactions. The proton-rich nuclides ^{58}Cu, ^{69}As, ^{90}Nb, ^{94}Rh, ^{105}Sn, and ^{118}Xe are chosen, which might be available for the neutron-deficient radioactive beams generated in the radioactive beam facilities. Figure 7 shows the production cross section of final fragments in collisions of ^{58}Cu, ^{69}As, ^{90}Nb, ^{94}Rh, ^{105}Sn, and ^{118}Xe on ^{238}U at incident energy $E_{\mathrm{lab}} = 6$ MeV/nucleon. It is obvious that the isotopic distribution width increases with the projectile mass. The solid color circles without open squares are the predicted new neutron-deficient isotopes that are listed in Table I. The unknown neutron-deficient isotope's proton number increases with increasing projectile mass. The calculation of the ^{118}Xe induced reaction shows that is is favorable for producing neutron-deficient isotopes $Z = 98$–100. The ^{94}Rh induced reaction is advantageous in producing neutron-deficient isotopes of $Z = 93$–97.

Figure 8 depicts the calculated evaporation residual cross sections for producing the neutron-deficient compound nucleus Pu from different projectile-target combinations through fusion-evaporation reactions. The black solid lines and pink dashed lines are the capture cross sections and fusion cross sections, respectively. One can see that the capture cross sections of the four systems are almost the same, because their Coulomb barriers are changing slightly. Their fusion cross sections are dropping rapidly with decreasing mass asymmetry caused by the higher inner barrier. In the figure, the black dashed line and black dash-dotted line are the $1n1\alpha$, $1n1p$ channels, respectively. The red solid line, red dashed line, and red dash-dotted line indicate $2n$, $2n1\alpha$, $2n1p$ channels, respectively. The green solid line, green dashed line, and green dash-dotted line are the $3n$, $3n1\alpha$, $3n1p$ channels, respectively. The blue solid line, blue dashed line, and blue dash-dotted line stand for $4n$, $4n1\alpha$, $4n1p$ channels, respectively. The combined channels with the charged particles are of significance in the decay process and are the main pathway for proton-rich nuclide production.

The calculated production cross sections of neutron-deficient actinide nuclei with $Z = 93$–100 through fusion-evaporation and multinucleon transfer reaction are in Fig. 9. The grey region indicates unknown neutron-deficient actinide isotopes. The black solid line and red solid line are $^{118}\mathrm{Xe} + ^{238}\mathrm{U}$ and $^{91}\mathrm{Tc} + ^{238}\mathrm{U}$ reactions, respectively. The reaction $^{91}\mathrm{Tc} + ^{238}\mathrm{U}$ has an advantage for producing unknown neutron-deficient nuclei with $Z = 93$–94, in comparsion of reaction $^{118}\mathrm{Xe} + ^{238}\mathrm{U}$, that is favorable to produce unknown neutron-deficient nuclei with $Z = 95$–100. The black solid square, green solid triangle, and blue solid square stand for pure neutron channels, neutron mixed proton channels, and neutron mixed alpha channels from ^{36}Ar induced fusion-evaporation reactions. From ^{36}Ar induced fusion-evaporation reactions, we found that synthesis of unknown neutron-deficient nuclei with $Z = 93$–94 prefer neutron mixed alpha channels, while pure neutron channels are favorable to producing unknown neutron-deficient nuclei with $Z = 95$–100. Through comparing the production cross sections via the fusion-evaporation and multinucleon transfer reactions, we found that fusion-evaporation reactions are still a promising

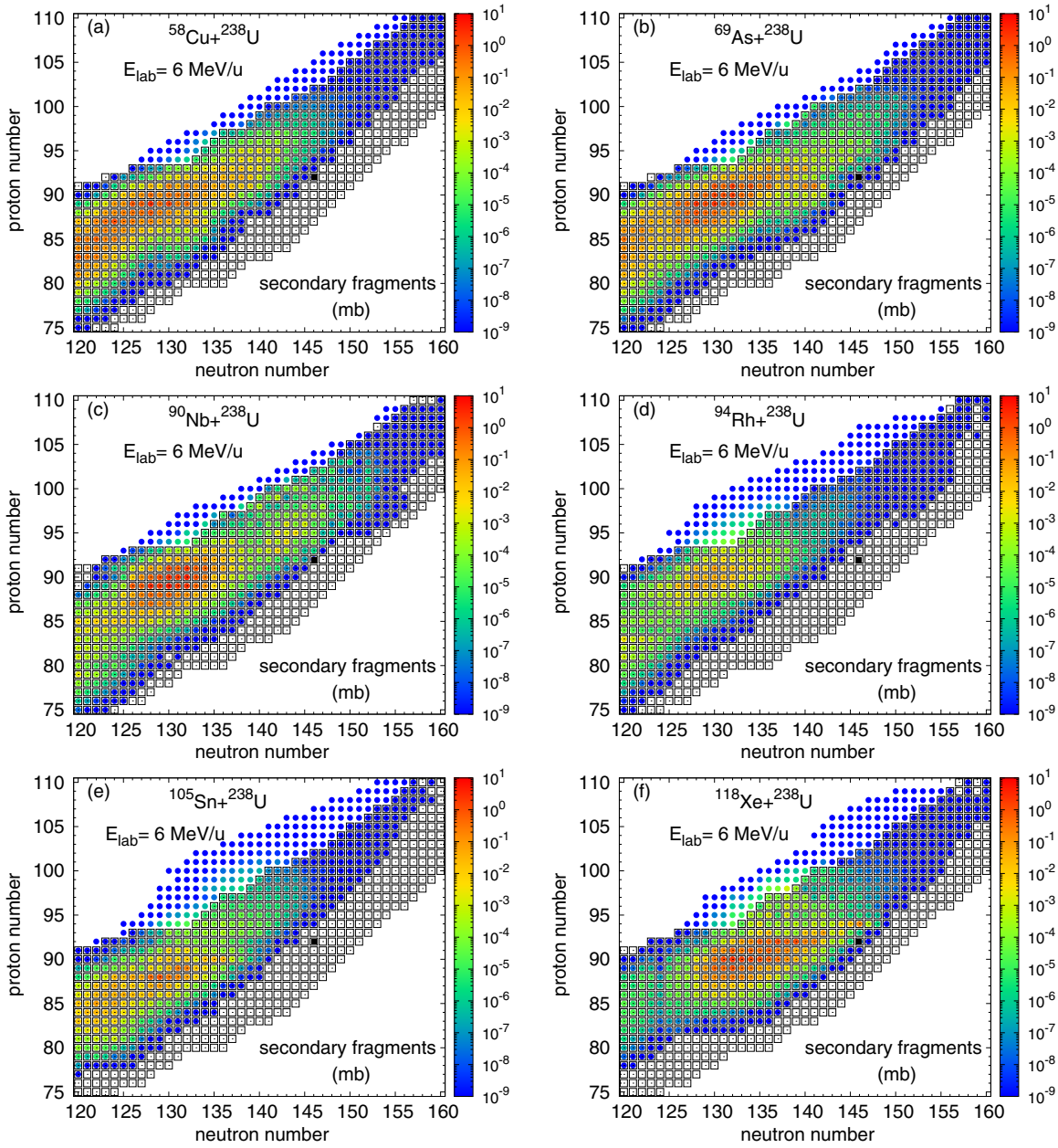

FIG. 7. Production cross sections of final products in the MNT reactions with (a) ^{58}Cu, (b) ^{69}As, (c) ^{90}Nb, (d) ^{94}Rh, (e) ^{105}Sn, and (f) ^{118}Xe on ^{238}U at the incident energy $E_{\rm lab} = 6$ MeV/nucleon. The entrance channels are marked by black solid squares.

way to produce neutron-deficient actinide nuclei. Moreover, the MNT reactions are favorable for creating the proton-rich isotopes within the large mass region.

The production cross sections of new neutron-deficient nuclei with $Z = 93$–100 are estimated via the fusion-evaporation reactions as shown in Tables II and III for the systems of ^{40}Ca, ^{36}Ar, ^{32}S, ^{28}Si, and^{24}Mg induced fusion reactions. For producing neutron-deficient actinide nuclei, the evaporation channels of charged particles play an important role in deexcitation processes. The products from charge evaporation channels are not very neutron deficient, in comparision with pure neutrons channels. The MNT reactions with neutron-deficient radioactive beams may also produce new neutron-deficient isotopes. The production cross section of new neutron-deficient nuclei from MNT reactions are equivalent to those from fusion-evaporation reactions, as shown in Table I. The production cross sections at the level of pb to mb are feasible for measurements in laboratories. New neutron-deficient nuclei produced through MNT reactions are broader, compared with the fusion-evaporation reactions. Further measurements are expected in the future experiments.

IV. CONCLUSIONS

In summary, the production of neutron-deficient actinide isotopes with charge numbers of $Z = 93$–100 has been thoroughly investigated within the DNS model through fusion-evaporation and multinucleon transfer reactions. For the MNT

TABLE I. Production cross sections of unknown neutron-deficient actinide isotopes with proton number Z and mass number A, predicted by the DNS model in the MNT reactions of ^{58}Cu + ^{238}U, ^{69}As + ^{238}U, ^{90}Nb + ^{238}U, ^{94}Rh + ^{238}U, ^{105}Sn + ^{238}U, and ^{118}Xe + ^{238}U around the Coulomb barrier energies. The symbol A is the mass number of product and the cross section is indicated in parentheses.

MNT	^{A}Np (mb)	^{A}Pu (mb)	^{A}Am (mb)	^{A}Cm (mb)	^{A}Bk (mb)	^{A}Cf (mb)	^{A}Es (mb)	^{A}Fm (mb)
^{58}Cu + ^{238}U	$^{225}(2\times10^{-4})$	$^{227}(8\times10^{-6})$	$^{229}(1\times10^{-6})$	$^{232}(2\times10^{-5})$	$^{233}(8\times10^{-7})$	$^{236}(1\times10^{-8})$	$^{240}(2\times10^{-8})$	$^{240}(<10^{-9})$
	$^{224}(1\times10^{-4})$	$^{226}(1\times10^{-6})$	$^{228}(8\times10^{-8})$	$^{231}(4\times10^{-6})$	$^{232}(8\times10^{-8})$	$^{235}(1\times10^{-9})$	$^{239}(5\times10^{-8})$	$^{239}(<10^{-9})$
	$^{223}(5\times10^{-5})$	$^{225}(2\times10^{-7})$	$^{227}(2\times10^{-8})$	$^{230}(6\times10^{-7})$	$^{231}(1\times10^{-8})$	$^{234}(<10^{-9})$	$^{238}(4\times10^{-9})$	$^{238}(<10^{-9})$
	$^{222}(2\times10^{-7})$	$^{224}(2\times10^{-8})$	$^{226}(1\times10^{-9})$	$^{229}(3\times10^{-8})$	$^{230}(<10^{-9})$	$^{233}(<10^{-9})$	$^{237}(<10^{-9})$	$^{237}(<10^{-9})$
	$^{221}(1\times10^{-7})$	$^{223}(3\times10^{-9})$	$^{225}(<10^{-9})$	$^{228}(2\times10^{-9})$	$^{229}(<10^{-9})$	$^{232}(<10^{-9})$	$^{236}(<10^{-9})$	$^{236}(<10^{-9})$
	$^{220}(6\times10^{-9})$	$^{222}(<10^{-9})$	$^{224}(<10^{-9})$	$^{227}(<10^{-9})$	$^{228}(<10^{-9})$	$^{231}(<10^{-9})$	$^{235}(<10^{-9})$	$^{235}(<10^{-9})$
^{69}As + ^{238}U	$^{225}(1\times10^{-3})$	$^{227}(2\times10^{-5})$	$^{229}(1\times10^{-5})$	$^{232}(4\times10^{-7})$	$^{233}(1\times10^{-6})$	$^{236}(5\times10^{-6})$	$^{240}(3\times10^{-8})$	$^{240}(1\times10^{-9})$
	$^{224}(2\times10^{-4})$	$^{226}(7\times10^{-6})$	$^{228}(5\times10^{-7})$	$^{231}(2\times10^{-7})$	$^{232}(<10^{-9})$	$^{235}(6\times10^{-8})$	$^{239}(8\times10^{-6})$	$^{239}(<10^{-9})$
	$^{223}(1\times10^{-4})$	$^{225}(1\times10^{-6})$	$^{227}(6\times10^{-7})$	$^{230}(2\times10^{-6})$	$^{231}(<10^{-9})$	$^{234}(<10^{-9})$	$^{238}(<10^{-9})$	$^{238}(<10^{-9})$
	$^{222}(4\times10^{-7})$	$^{224}(6\times10^{-8})$	$^{226}(2\times10^{-9})$	$^{229}(1\times10^{-9})$	$^{230}(<10^{-9})$	$^{233}(<10^{-9})$	$^{237}(<10^{-9})$	$^{237}(<10^{-9})$
	$^{221}(2\times10^{-7})$	$^{223}(6\times10^{-9})$	$^{225}(<10^{-9})$	$^{228}(<10^{-9})$	$^{229}(<10^{-9})$	$^{232}(<10^{-9})$	$^{236}(<10^{-9})$	$^{236}(<10^{-9})$
	$^{220}(1\times10^{-8})$	$^{222}(<10^{-9})$	$^{224}(<10^{-9})$	$^{227}(<10^{-9})$	$^{228}(<10^{-9})$	$^{231}(<10^{-9})$	$^{235}(<10^{-9})$	$^{235}(<10^{-9})$
	$^{219}(1\times10^{-9})$	$^{221}(<10^{-9})$	$^{223}(<10^{-9})$	$^{226}(<10^{-9})$	$^{227}(<10^{-9})$	$^{230}(<10^{-9})$	$^{234}(<10^{-9})$	$^{234}(<10^{-9})$
	$^{218}(<10^{-9})$	$^{220}(<10^{-9})$	$^{222}(<10^{-9})$	$^{225}(<10^{-9})$	$^{226}(<10^{-9})$	$^{229}(<10^{-9})$	$^{233}(<10^{-9})$	$^{233}(<10^{-9})$
^{90}Nb + ^{238}U	$^{225}(7\times10^{-3})$	$^{227}(2\times10^{-5})$	$^{229}(4\times10^{-6})$	$^{232}(2\times10^{-7})$	$^{233}(1\times10^{-5})$	$^{236}(1\times10^{-6})$	$^{240}(5\times10^{-5})$	$^{240}(<10^{-9})$
	$^{224}(2\times10^{-4})$	$^{226}(5\times10^{-6})$	$^{228}(3\times10^{-7})$	$^{231}(7\times10^{-8})$	$^{232}(1\times10^{-7})$	$^{235}(<10^{-9})$	$^{239}(6\times10^{-6})$	$^{239}(<10^{-9})$
	$^{223}(1\times10^{-4})$	$^{225}(2\times10^{-6})$	$^{227}(8\times10^{-7})$	$^{230}(9\times10^{-7})$	$^{231}(<10^{-9})$	$^{234}(<10^{-9})$	$^{238}(5\times10^{-8})$	$^{238}(<10^{-9})$
	$^{222}(1\times10^{-6})$	$^{224}(8\times10^{-6})$	$^{226}(5\times10^{-9})$	$^{229}(1\times10^{-9})$	$^{230}(<10^{-9})$	$^{233}(<10^{-9})$	$^{237}(<10^{-9})$	$^{237}(<10^{-9})$
	$^{221}(1\times10^{-6})$	$^{223}(1\times10^{-7})$	$^{225}(<10^{-9})$	$^{228}(<10^{-9})$	$^{229}(<10^{-9})$	$^{232}(<10^{-9})$	$^{236}(<10^{-9})$	$^{236}(<10^{-9})$
	$^{220}(1\times10^{-8})$	$^{222}(2\times10^{-8})$	$^{224}(<10^{-9})$	$^{227}(<10^{-9})$	$^{228}(<10^{-9})$	$^{231}(<10^{-9})$	$^{235}(<10^{-9})$	$^{235}(<10^{-9})$
	$^{219}(6\times10^{-9})$	$^{221}(<10^{-9})$	$^{223}(<10^{-9})$	$^{226}(<10^{-9})$	$^{227}(<10^{-9})$	$^{230}(<10^{-9})$	$^{234}(<10^{-9})$	$^{234}(<10^{-9})$
	$^{218}(<10^{-9})$	$^{220}(<10^{-9})$	$^{222}(<10^{-9})$	$^{225}(<10^{-9})$	$^{226}(<10^{-9})$	$^{229}(<10^{-9})$	$^{233}(<10^{-9})$	$^{233}(<10^{-9})$
^{94}Rh + ^{238}U	$^{225}(9\times10^{-4})$	$^{227}(7\times10^{-5})$	$^{229}(6\times10^{-5})$	$^{232}(5\times10^{-6})$	$^{233}(1\times10^{-6})$	$^{236}(3\times10^{-8})$	$^{240}(1\times10^{-8})$	$^{240}(<10^{-9})$
	$^{224}(1\times10^{-3})$	$^{226}(1\times10^{-4})$	$^{228}(1\times10^{-5})$	$^{231}(2\times10^{-6})$	$^{232}(7\times10^{-7})$	$^{235}(1\times10^{-7})$	$^{239}(5\times10^{-9})$	$^{239}(<10^{-9})$
	$^{223}(1\times10^{-3})$	$^{225}(7\times10^{-5})$	$^{227}(2\times10^{-5})$	$^{230}(6\times10^{-6})$	$^{231}(1\times10^{-6})$	$^{234}(2\times10^{-7})$	$^{238}(<10^{-9})$	$^{238}(<10^{-9})$
	$^{222}(3\times10^{-5})$	$^{224}(2\times10^{-5})$	$^{226}(4\times10^{-6})$	$^{229}(1\times10^{-6})$	$^{230}(1\times10^{-7})$	$^{233}(4\times10^{-8})$	$^{237}(1\times10^{-8})$	$^{237}(<10^{-9})$
	$^{221}(3\times10^{-5})$	$^{223}(8\times10^{-6})$	$^{225}(2\times10^{-6})$	$^{228}(1\times10^{-6})$	$^{229}(7\times10^{-8})$	$^{232}(1\times10^{-8})$	$^{236}(4\times10^{-9})$	$^{236}(<10^{-9})$
	$^{220}(1\times10^{-6})$	$^{222}(2\times10^{-7})$	$^{224}(6\times10^{-8})$	$^{227}(1\times10^{-7})$	$^{228}(5\times10^{-9})$	$^{231}(2\times10^{-9})$	$^{235}(6\times10^{-9})$	$^{235}(<10^{-9})$
	$^{219}(1\times10^{-8})$	$^{221}(1\times10^{-8})$	$^{223}(2\times10^{-8})$	$^{226}(6\times10^{-8})$	$^{227}(<10^{-9})$	$^{230}(<10^{-9})$	$^{234}(1\times10^{-9})$	$^{234}(<10^{-9})$
	$^{218}(<10^{-9})$	$^{220}(<10^{-9})$	$^{222}(<10^{-9})$	$^{225}(<10^{-9})$	$^{226}(<10^{-9})$	$^{229}(<10^{-9})$	$^{233}(<10^{-9})$	$^{233}(<10^{-9})$
^{105}Sn + ^{238}U	$^{225}(1\times10^{-4})$	$^{227}(9\times10^{-5})$	$^{229}(7\times10^{-6})$	$^{232}(2\times10^{-5})$	$^{233}(3\times10^{-6})$	$^{236}(2\times10^{-6})$	$^{240}(8\times10^{-8})$	$^{240}(1\times10^{-7})$
	$^{224}(5\times10^{-5})$	$^{226}(2\times10^{-5})$	$^{228}(9\times10^{-7})$	$^{231}(6\times10^{-6})$	$^{232}(2\times10^{-8})$	$^{235}(6\times10^{-7})$	$^{239}(8\times10^{-7})$	$^{239}(1\times10^{-7})$
	$^{223}(1\times10^{-4})$	$^{225}(1\times10^{-5})$	$^{227}(5\times10^{-7})$	$^{230}(3\times10^{-7})$	$^{231}(7\times10^{-9})$	$^{234}(9\times10^{-7})$	$^{238}(3\times10^{-7})$	$^{238}(1\times10^{-7})$
	$^{222}(4\times10^{-7})$	$^{224}(3\times10^{-6})$	$^{226}(9\times10^{-8})$	$^{229}(6\times10^{-8})$	$^{230}(<10^{-9})$	$^{233}(1\times10^{-7})$	$^{237}(6\times10^{-7})$	$^{237}(3\times10^{-8})$
	$^{221}(3\times10^{-7})$	$^{223}(3\times10^{-7})$	$^{225}(4\times10^{-8})$	$^{228}(1\times10^{-8})$		$^{232}(7\times10^{-8})$	$^{236}(1\times10^{-7})$	$^{236}(2\times10^{-8})$
	$^{220}(<10^{-9})$	$^{222}(8\times10^{-9})$	$^{224}(<10^{-9})$	$^{227}(2\times10^{-9})$		$^{231}(<10^{-9})$	$^{235}(1\times10^{-7})$	$^{235}(2\times10^{-9})$
		$^{221}(<10^{-9})$		$^{226}(<10^{-9})$			$^{234}(1\times10^{-8})$	$^{234}(<10^{-9})$
							$^{233}(7\times10^{-9})$	
							$^{232}(<10^{-9})$	
^{118}Xe + ^{238}U	$^{225}(2\times10^{-4})$	$^{227}(2\times10^{-5})$	$^{229}(2\times10^{-4})$	$^{232}(2\times10^{-4})$	$^{233}(9\times10^{-5})$	$^{236}(9\times10^{-4})$	$^{240}(3\times10^{-6})$	$^{240}(2\times10^{-6})$
	$^{224}(2\times10^{-5})$	$^{226}(3\times10^{-5})$	$^{228}(1\times10^{-5})$	$^{231}(6\times10^{-6})$	$^{232}(3\times10^{-6})$	$^{235}(8\times10^{-5})$	$^{239}(1\times10^{-5})$	$^{239}(5\times10^{-7})$
	$^{223}(4\times10^{-5})$	$^{225}(5\times10^{-7})$	$^{227}(8\times10^{-6})$	$^{230}(1\times10^{-5})$	$^{231}(1\times10^{-6})$	$^{234}(5\times10^{-5})$	$^{238}(1\times10^{-6})$	$^{238}(3\times10^{-7})$
	$^{222}(5\times10^{-8})$	$^{224}(4\times10^{-7})$	$^{226}(9\times10^{-8})$	$^{229}(4\times10^{-7})$	$^{230}(1\times10^{-8})$	$^{233}(2\times10^{-6})$	$^{237}(1\times10^{-6})$	$^{237}(<10^{-9})$
	$^{221}(1\times10^{-8})$	$^{223}(4\times10^{-9})$	$^{225}(4\times10^{-8})$	$^{228}(8\times10^{-7})$	$^{229}(8\times10^{-8})$	$^{232}(<10^{-9})$	$^{236}(5\times10^{-7})$	
	$^{220}(<10^{-9})$	$^{222}(<10^{-9})$	$^{224}(<10^{-9})$	$^{227}(<10^{-9})$	$^{228}(<10^{-9})$		$^{235}(9\times10^{-7})$	
							1×10^{-8}	
							$<10^{-9}$	

reactions, the systems of ^{105,110,115,120,125,130}Sn ^{58}Cu, ^{69}As, ^{90}Nb, ^{94}Rh, and ^{118}Xe bombarding ^{238}U around Coulomb barrier energies are chosen. The ^{40}Ca, ^{36}Ar, ^{32}S, ^{28}Si, and ^{24}Mg induced fusion reactions are selected for comparison. The valley shape of the PES influences the formation of primary fragments and leads to the production of neutron-deficient isotopes. The deexcitation process shifts the proton excess of fragments towards the β-stability line. The isospin relaxation in the nucleon transfer is coupled to the dissipation of relative energy and angular momentum of the colliding system. The

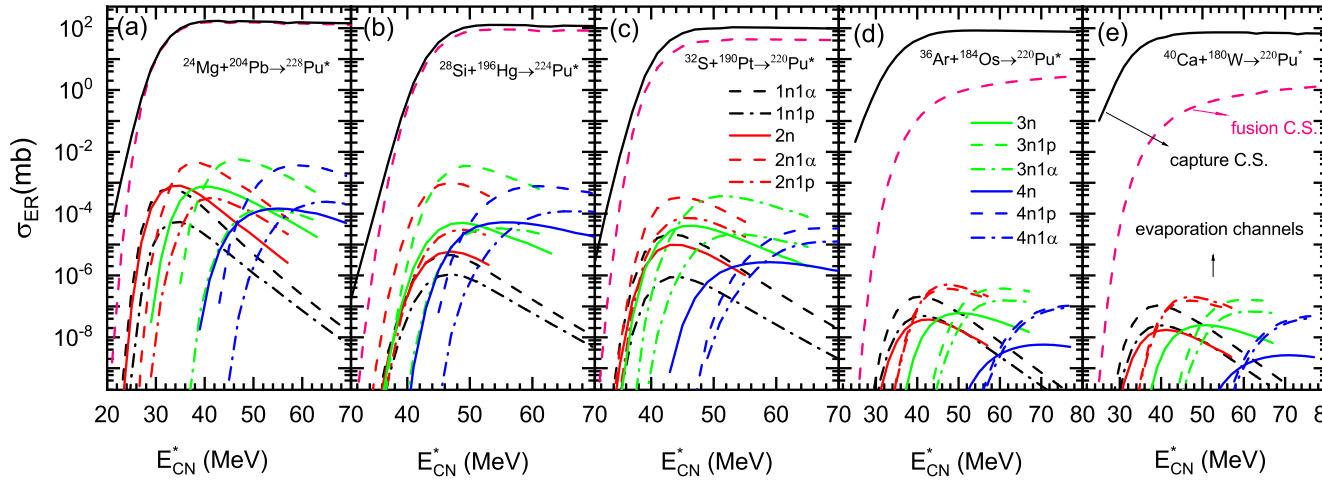

FIG. 8. The fusion-evaporation reactions of (a) ^{24}Mg + ^{204}Pb, (b) ^{28}Si + ^{196}Hg, (c) ^{32}S + ^{190}Pt, (d) ^{36}Ar + ^{184}Os, and (e) ^{40}Ca + ^{180}W for producing the same compound nuclide Pu. The solid color lines, dashed lines, and dot-dashed lines are the pure neutron, neutron mixed proton, and neutron mixed alpha channels, respectively.

fragment yields are associated with nuclear shapes of the colliding nuclei and details of the potential energy surface in the MNT reactions.

Production of proton-rich actinide isotopes relies strongly on the projectile-target mass asymmetry in the FE reactions. The charged particle evaporation channels play an important role in final production cross sections. The anisotropy emission of MNT fragments is associated with the incident energy and deformation of colliding system. The angular distribution of the PLFs is shifted to the forward region with increasing Coulomb barrier. However, that of TLFs exhibits an opposite trend. The total kinetic energies and angular spectra of primary fragments are highly dependent on colliding orientations. The distribution width for transferring neutrons

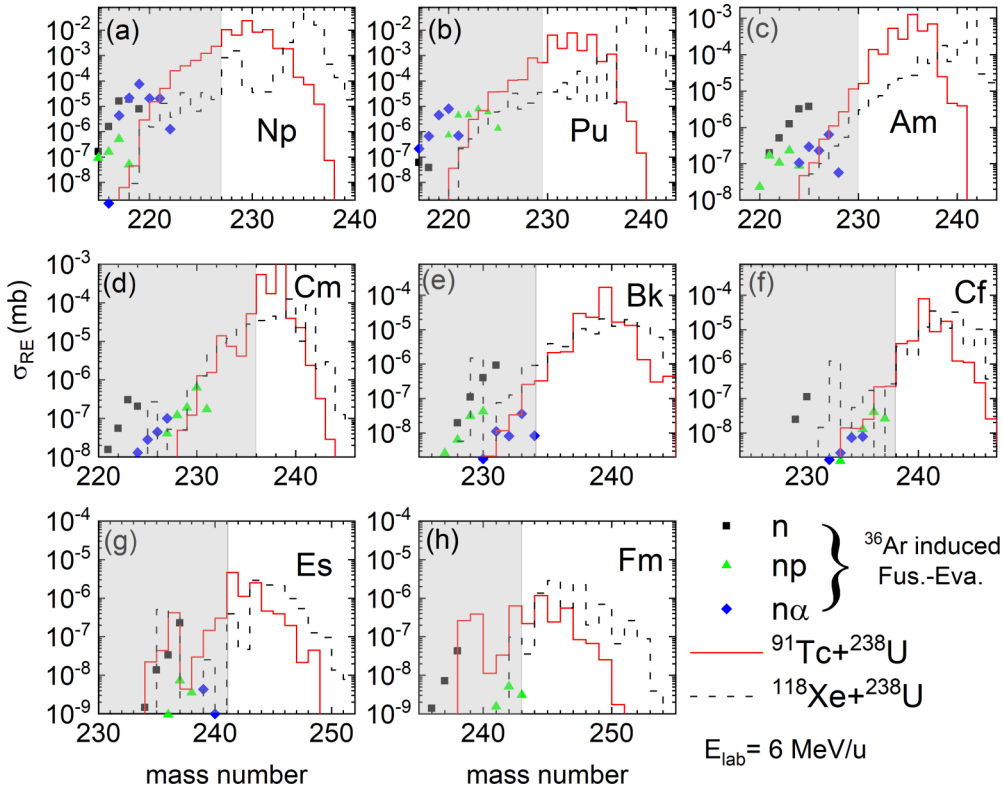

FIG. 9. Comparison of the isotopic distributions of (a) Np, (b) Pu, (c) Am, (d) Cm, (e) Bk, (f) Cf, (g) Es, and (h) Fm in the MNT reactions of ^{91}Tc + ^{238}U and ^{118}Xe + ^{238}U. The black, green, and blue points stand for the pure neutron channels, neutron-proton mixing channels, and alpha-neutron mixing channels in ^{36}Ar induced fusion-evaporation reactions.

TABLE II. Cross sections of unknown proton-rich actinide isotopes with $Z = 93$–100 predicted by the DNS model in fusion-evaporation reactions, for the ^{40}Ca, ^{36}Ar, ^{32}S induced reactions with targets of ^{181}Ta, ^{180}W, ^{185}Re, ^{184}Os, ^{191}Ir, ^{190}Pt, ^{197}Au, ^{196}Hg, ^{203}Tl, ^{204}Pb, ^{209}Bi. The evaporation channels are listed in the first column. The projectiles and targets are listed in the same rows.

FE	^{A}Np (mb)	^{A}Pu (mb)	^{A}Am (mb)	^{A}Cm (mb)	^{A}Bk (mb)	^{A}Cf (mb)	^{A}Es (mb)	^{A}Fm (mb)
^{40}Ca+	^{181}Ta	^{180}W	^{185}Re	^{184}Os	^{191}Ir	^{190}Pt	^{197}Au	^{196}Hg
$2n$	$^{219}(1\times10^{-6})$	$^{218}(1\times10^{-8})$	$^{223}(6\times10^{-8})$	$^{222}(4\times10^{-9})$	$^{229}(5\times10^{-7})$	$^{228}(7\times10^{-9})$	$^{235}(1\times10^{-7})$	$^{234}(2\times10^{-8})$
$3n$	$^{218}(3\times10^{-6})$	$^{217}(2\times10^{-8})$	$^{222}(6\times10^{-8})$	$^{221}(2\times10^{-9})$	$^{228}(7\times10^{-8})$	$^{227}(2\times10^{-9})$	$^{234}(1\times10^{-8})$	$^{233}(1\times10^{-9})$
$4n$	$^{217}(4\times10^{-6})$	$^{216}(2\times10^{-9})$	$^{221}(8\times10^{-8})$	$^{220}(<10^{-9})$	$^{227}(1\times10^{-8})$		$^{233}(4\times10^{-9})$	$^{232}(<10^{-9})$
$5n$	$^{216}(5\times10^{-7})$	$^{215}(<10^{-9})$	$^{220}(1\times10^{-8})$		$^{226}(2\times10^{-9})$		$^{232}(<10^{-9})$	
$6n$	$^{215}(6\times10^{-8})$		$^{219}(1\times10^{-9})$		$^{225}(<10^{-6})$			
^{40}Ca+	^{180}W	^{185}Re	^{184}Os	^{191}Ir	^{190}Pt	^{197}Au	^{196}Hg	^{203}Tl
$1n1p$	$^{218}(2\times10^{-8})$	$^{223}(5\times10^{-8})$	$^{222}(1\times10^{-9})$	$^{229}(1\times10^{-7})$	$^{228}(8\times10^{-9})$	$^{235}(2\times10^{-8})$	$^{234}(6\times10^{-9})$	$^{241}(1\times10^{-9})$
$2n1p$	$^{217}(1\times10^{-7})$	$^{222}(1\times10^{-7})$	$^{221}(6\times10^{-9})$	$^{228}(1\times10^{-7})$	$^{227}(<10^{-9})$	$^{234}(2\times10^{-8})$	$^{233}(2\times10^{-9})$	$^{240}(1\times10^{-9})$
$3n1p$	$^{216}(2\times10^{-7})$	$^{221}(2\times10^{-7})$	$^{220}(2\times10^{-9})$	$^{227}(5\times10^{-8})$		$^{233}(5\times10^{-9})$	$^{232}(<10^{-9})$	$^{239}(<10^{-9})$
$4n1p$	$^{215}(6\times10^{-8})$	$^{220}(3\times10^{-7})$	$^{219}(2\times10^{-9})$	$^{226}(2\times10^{-8})$		$^{232}(<10^{-9})$		
$5n1p$	$^{214}(4\times10^{-8})$	$^{219}(2\times10^{-7})$	$^{218}(<10^{-9})$	$^{225}(8\times10^{-9})$				
^{40}Ca+	^{185}Re	^{184}Os	^{191}Ir	^{190}Pt	^{197}Au	^{196}Hg	^{203}Tl	^{204}Pb
$1n1\alpha$	$^{220}(4\times10^{-8})$	$^{219}(3\times10^{-8})$	$^{226}(8\times10^{-8})$	$^{225}(2\times10^{-8})$	$^{232}(8\times10^{-9})$	$^{231}(1\times10^{-8})$	$^{239}(<10^{-9})$	$^{239}(1\times10^{-9})$
$2n1\alpha$	$^{219}(2\times10^{-6})$	$^{218}(1\times10^{-8})$	$^{225}(1\times10^{-7})$	$^{224}(1\times10^{-8})$	$^{231}(2\times10^{-8})$	$^{230}(1\times10^{-9})$	$^{238}(1\times10^{-9})$	$^{238}(<10^{-9})$
$3n1\alpha$	$^{218}(1\times10^{-6})$	$^{217}(1\times10^{-8})$	$^{224}(5\times10^{-8})$	$^{223}(1\times10^{-8})$	$^{230}(3\times10^{-9})$	$^{229}(<10^{-9})$	$^{237}(<10^{-9})$	
$4n1\alpha$	$^{217}(1\times10^{-6})$	$^{216}(3\times10^{-9})$	$^{223}(2\times10^{-8})$	$^{222}(6\times10^{-9})$	$^{229}(<10^{-9})$	<		
$5n1\alpha$	$^{216}(2\times10^{-7})$	$^{215}(<10^{-9})$	$^{222}(8\times10^{-9})$	$^{221}(1\times10^{-9})$				
$5n1\alpha$	$^{215}(6\times10^{-9})$		$^{221}(<10^{-9})$	$^{220}(<10^{-9})$				
^{36}Ar+	^{185}Re	^{184}Os	^{191}Ir	^{190}Pt	^{197}Au	^{196}Hg	^{203}Tl	^{204}Pb
$2n$	$^{219}(7\times10^{-6})$	$^{218}(3\times10^{-8})$	$^{225}(3\times10^{-6})$	$^{224}(2\times10^{-7})$	$^{231}(9\times10^{-7})$	$^{230}(1\times10^{-7})$	$^{237}(2\times10^{-7})$	$^{238}(4\times10^{-8})$
$3n$	$^{218}(1\times10^{-5})$	$^{217}(6\times10^{-8})$	$^{224}(3\times10^{-6})$	$^{223}(3\times10^{-7})$	$^{230}(4\times10^{-7})$	$^{229}(2\times10^{-8})$	$^{236}(3\times10^{-8})$	$^{237}(7\times10^{-9})$
$4n$	$^{217}(1\times10^{-5})$	$^{216}(5\times10^{-9})$	$^{223}(1\times10^{-6})$	$^{222}(5\times10^{-8})$	$^{229}(1\times10^{-7})$	$^{228}(1\times10^{-9})$	$^{235}(1\times10^{-8})$	$^{236}(1\times10^{-9})$
$5n$	$^{216}(1\times10^{-6})$	$^{215}(<10^{-9})$	$^{222}(5\times10^{-7})$	$^{221}(1\times10^{-8})$	$^{228}(1\times10^{-8})$	$^{227}(<10^{-9})$	$^{234}(1\times10^{-9})$	$^{235}(<10^{-9})$
$6n$	$^{215}(1\times10^{-7})$		$^{221}(1\times10^{-7})$	$^{220}(<10^{-9})$	$^{227}(<10^{-9})$		$^{233}(<10^{-9})$	
^{36}Ar+	^{184}Os	^{191}Ir	^{190}Pt	^{197}Au	^{196}Hg	^{203}Tl	^{204}Pb	^{209}Bi
$1n1p$	$^{218}(5\times10^{-8})$	$^{225}(1\times10^{-6})$	$^{224}(8\times10^{-8})$	$^{231}(1\times10^{-7})$	$^{230}(4\times10^{-8})$	$^{237}(2\times10^{-8})$	$^{238}(3\times10^{-9})$	$^{243}(3\times10^{-9})$
$2n1p$	$^{217}(5\times10^{-7})$	$^{224}(5\times10^{-6})$	$^{223}(2\times10^{-7})$	$^{230}(6\times10^{-7})$	$^{229}(3\times10^{-8})$	$^{236}(4\times10^{-8})$	$^{237}(7\times10^{-9})$	$^{242}(5\times10^{-9})$
$3n1p$	$^{216}(1\times10^{-7})$	$^{223}(7\times10^{-6})$	$^{222}(1\times10^{-7})$	$^{229}(1\times10^{-7})$	$^{228}(6\times10^{-9})$	$^{235}(1\times10^{-8})$	$^{236}(<10^{-9})$	$^{241}(1\times10^{-9})$
$4n1p$	$^{215}(9\times10^{-8})$	$^{222}(4\times10^{-6})$	$^{221}(1\times10^{-7})$	$^{228}(1\times10^{-7})$	$^{227}(2\times10^{-9})$	$^{234}(7\times10^{-9})$		$^{240}(<10^{-9})$
$5n1p$	$^{214}(5\times10^{-9})$	$^{221}(4\times10^{-6})$	$^{220}(2\times10^{-8})$	$^{227}(4\times10^{-8})$	$^{226}(<10^{-9})$	$^{233}(1\times10^{-9})$		
^{36}Ar+	^{191}Ir	^{190}Pt	^{197}Au	^{196}Hg	^{203}Tl	^{204}Pb	^{209}Bi	
$1n1\alpha$	$^{222}(1\times10^{-6})$	$^{221}(7\times10^{-7})$	$^{228}(5\times10^{-8})$	$^{227}(1\times10^{-7})$	$^{234}(8\times10^{-9})$	$^{235}(7\times10^{-9})$	$^{240}(1\times10^{-9})$	
$2n1\alpha$	$^{221}(2\times10^{-5})$	$^{220}(8\times10^{-6})$	$^{227}(6\times10^{-7})$	$^{226}(4\times10^{-8})$	$^{233}(3\times10^{-8})$	$^{234}(7\times10^{-9})$	$^{239}(4\times10^{-9})$	
$3n1\alpha$	$^{220}(2\times10^{-5})$	$^{219}(4\times10^{-6})$	$^{226}(2\times10^{-7})$	$^{225}(2\times10^{-8})$	$^{232}(8\times10^{-9})$	$^{233}(4\times10^{-6})$	$^{238}(<10^{-9})$	
$4n1\alpha$	$^{219}(7\times10^{-5})$	$^{218}(6\times10^{-7})$	$^{225}(2\times10^{-7})$	$^{224}(1\times10^{-8})$	$^{231}(1\times10^{-8})$	$^{232}(2\times10^{-9})$		
$5n1\alpha$	$^{218}(2\times10^{-5})$	$^{217}(2\times10^{-7})$	$^{224}(1\times10^{-7})$	$^{223}(5\times10^{-9})$	$^{230}(1\times10^{-9})$	$^{231}(1\times10^{-9})$		
$5n1\alpha$	$^{217}(4\times10^{-6})$	$^{216}(1\times10^{-7})$	$^{223}(5\times10^{-9})$	$^{222}(<10^{-9})$	$^{229}(<10^{-9})$	$^{230}(<10^{-9})$		
^{32}S+	^{191}Ir	^{190}Pt	^{197}Au	^{196}Hg	^{203}Tl	^{204}Pb	^{209}Bi	
$2n$	$^{221}(6\times10^{-5})$	$^{220}(9\times10^{-6})$	$^{227}(1\times10^{-5})$	$^{226}(1\times10^{-6})$	$^{233}(1\times10^{-5})$	$^{234}(1\times10^{-6})$	$^{239}(3\times10^{-7})$	
$3n$	$^{220}(3\times10^{-4})$	$^{219}(4\times10^{-5})$	$^{226}(1\times10^{-5})$	$^{225}(1\times10^{-6})$	$^{232}(1\times10^{-6})$	$^{233}(3\times10^{-7})$	$^{238}(8\times10^{-8})$	
$4n$	$^{219}(1\times10^{-3})$	$^{218}(2\times10^{-6})$	$^{225}(7\times10^{-6})$	$^{224}(1\times10^{-7})$	$^{231}(6\times10^{-7})$	$^{232}(4\times10^{-8})$	$^{237}(4\times10^{-8})$	
$5n$	$^{218}(1\times10^{-4})$	$^{217}(6\times10^{-7})$	$^{224}(1\times10^{-6})$	$^{223}(9\times10^{-8})$	$^{230}(1\times10^{-7})$	$^{231}(9\times10^{-9})$	$^{236}(5\times10^{-9})$	
$6n$	$^{217}(6\times10^{-5})$	$^{216}(5\times10^{-9})$	$^{223}(4\times10^{-7})$	$^{222}(4\times10^{-9})$	$^{229}(1\times10^{-8})$	$^{230}(<10^{-9})$	$^{235}(<10^{-9})$	
^{32}S+	^{190}Pt	^{197}Au	^{196}Hg	^{203}Tl	^{204}Pb	^{209}Bi		
$1n1p$	$^{220}(8\times10^{-7})$	$^{227}(2\times10^{-6})$	$^{226}(5\times10^{-7})$	$^{233}(1\times10^{-6})$	$^{234}(1\times10^{-7})$	$^{239}(2\times10^{-8})$		
$2n1p$	$^{219}(7\times10^{-5})$	$^{226}(2\times10^{-5})$	$^{225}(1\times10^{-6})$	$^{232}(2\times10^{-6})$	$^{233}(2\times10^{-7})$	$^{238}(6\times10^{-8})$		
$3n1p$	$^{218}(2\times10^{-5})$	$^{225}(1\times10^{-5})$	$^{224}(3\times10^{-7})$	$^{231}(8\times10^{-7})$	$^{232}(3\times10^{-8})$	$^{237}(2\times10^{-8})$		
$4n1p$	$^{217}(1\times10^{-5})$	$^{224}(1\times10^{-5})$	$^{223}(2\times10^{-7})$	$^{230}(5\times10^{-7})$	$^{231}(4\times10^{-8})$	$^{236}(1\times10^{-8})$		
$5n1p$	$^{216}(1\times10^{-5})$	$^{223}(1\times10^{-5})$	$^{222}(1\times10^{-7})$	$^{229}(1\times10^{-7})$	$^{230}(5\times10^{-9})$	$^{235}(5\times10^{-9})$		
$6n1p$	$^{215}(1\times10^{-8})$	$^{222}(1\times10^{-6})$	$^{221}(5\times10^{-9})$	$^{228}(2\times10^{-9})$	$^{229}(<10^{-9})$	$^{234}(<10^{-9})$		
^{32}S+	^{197}Au	^{196}Hg	^{203}Tl	^{204}Pb	^{209}Bi			
$1n1\alpha$	$^{224}(1\times10^{-6})$	$^{223}(4\times10^{-6})$	$^{230}(4\times10^{-7})$	$^{231}(4\times10^{-7})$	$^{236}(8\times10^{-9})$			
$2n1\alpha$	$^{223}(6\times10^{-5})$	$^{222}(1\times10^{-5})$	$^{229}(2\times10^{-6})$	$^{230}(4\times10^{-7})$	$^{235}(5\times10^{-8})$			
$3n1\alpha$	$^{222}(6\times10^{-5})$	$^{221}(8\times10^{-6})$	$^{228}(6\times10^{-7})$	$^{229}(1\times10^{-7})$	$^{234}(1\times10^{-8})$			

TABLE II. *(Continued.)*

FE	^{A}Np (mb)	^{A}Pu (mb)	^{A}Am (mb)	^{A}Cm (mb)	^{A}Bk (mb)	^{A}Cf (mb)	^{A}Es (mb)	^{A}Fm (mb)
$4n1\alpha$	$^{221}(7\times10^{-5})$	$^{220}(8\times10^{-6})$	$^{227}(1\times10^{-6})$	$^{228}(8\times10^{-8})$	$^{233}(1\times10^{-8})$			
$5n1\alpha$	$^{220}(4\times10^{-5})$	$^{219}(4\times10^{-6})$	$^{226}(3\times10^{-7})$	$^{227}(3\times10^{-8})$	$^{232}(2\times10^{-8})$			
$5n1\alpha$	$^{219}(6\times10^{-5})$	$^{218}(1\times10^{-7})$	$^{225}(3\times10^{-8})$	$^{226}(<10^{-9})$	$^{231}(6\times10^{-9})$			
$6n1\alpha$	$^{218}(2\times10^{-7})$	$^{217}(<10^{-9})$	$^{224}(<10^{-9})$		$^{230}(<10^{-9})$			

TABLE III. Same as Table II, but for the ^{28}Si, ^{24}Mg induced reactions.

FE	^{A}Np (mb)	^{A}Pu (mb)	^{A}Am (mb)	^{A}Cm (mb)	^{A}Bk (mb)	^{A}Cf (mb)	^{A}Es (mb)	^{A}Fm (mb)
^{28}Si+	^{197}Au	^{196}Hg	^{203}Tl	^{204}Pb	^{209}Bi			
$2n$	$^{223}(2\times10^{-5})$	$^{222}(5\times10^{-6})$	$^{229}(3\times10^{-5})$	$^{230}(1\times10^{-5})$	$^{235}(4\times10^{-6})$			
$3n$	$^{222}(3\times10^{-4})$	$^{221}(5\times10^{-5})$	$^{228}(5\times10^{-5})$	$^{229}(7\times10^{-6})$	$^{234}(4\times10^{-6})$			
$4n$	$^{221}(1\times10^{-3})$	$^{220}(5\times10^{-5})$	$^{227}(3\times10^{-5})$	$^{228}(1\times10^{-6})$	$^{233}(2\times10^{-6})$			
$5n$	$^{220}(3\times10^{-4})$	$^{219}(1\times10^{-5})$	$^{226}(7\times10^{-6})$	$^{227}(5\times10^{-7})$	$^{232}(3\times10^{-7})$			
$6n$	$^{219}(9\times10^{-4})$	$^{218}(8\times10^{-7})$	$^{225}(2\times10^{-6})$	$^{226}(2\times10^{-8})$	$^{231}(9\times10^{-8})$			
$7n$	$^{218}(2\times10^{-5})$	$^{217}(<10^{-9})$	$^{224}(1\times10^{-8})$	$^{225}(<10^{-9})$	$^{230}(<10^{-9})$			
^{28}Si+	^{196}Hg	^{203}Tl	^{204}Pb	^{209}Bi				
$1n1p$	$^{222}(1\times10^{-6})$	$^{229}(3\times10^{-6})$	$^{230}(8\times10^{-7})$	$^{235}(3\times10^{-7})$				
$2n1p$	$^{221}(3\times10^{-5})$	$^{228}(4\times10^{-5})$	$^{229}(6\times10^{-6})$	$^{234}(2\times10^{-6})$				
$3n1p$	$^{220}(3\times10^{-5})$	$^{227}(5\times10^{-5})$	$^{228}(1\times10^{-6})$	$^{233}(1\times10^{-6})$				
$4n1p$	$^{219}(1\times10^{-4})$	$^{226}(3\times10^{-5})$	$^{227}(2\times10^{-6})$	$^{232}(1\times10^{-6})$				
$5n1p$	$^{218}(2\times10^{-5})$	$^{225}(3\times10^{-5})$	$^{226}(6\times10^{-7})$	$^{231}(7\times10^{-7})$				
$6n1p$	$^{217}(3\times10^{-6})$	$^{224}(5\times10^{-6})$	$^{225}(3\times10^{-8})$	$^{230}(3\times10^{-8})$				
^{28}Si+	^{203}Tl	^{204}Pb	^{209}Bi					
$1n1\alpha$	$^{226}(2\times10^{-6})$	$^{227}(3\times10^{-6})$	$^{232}(1\times10^{-7})$					
$2n1\alpha$	$^{225}(1\times10^{-4})$	$^{226}(1\times10^{-5})$	$^{231}(3\times10^{-6})$					
$3n1\alpha$	$^{224}(1\times10^{-4})$	$^{225}(1\times10^{-5})$	$^{230}(1\times10^{-6})$					
$4n1\alpha$	$^{223}(1\times10^{-4})$	$^{224}(1\times10^{-5})$	$^{229}(2\times10^{-6})$					
$5n1\alpha$	$^{222}(1\times10^{-4})$	$^{223}(1\times10^{-5})$	$^{228}(1\times10^{-6})$					
$6n1\alpha$	$^{221}(6\times10^{-5})$	$^{222}(1\times10^{-6})$	$^{227}(1\times10^{-7})$					
$7n1\alpha$	$^{220}(1\times10^{-6})$	$^{221}(6\times10^{-9})$	$^{226}(<10^{-9})$					
^{24}Mg+	^{203}Tl	^{204}Pb	^{209}Bi					
$2n$	$^{225}(2\times10^{-3})$	$^{226}(8\times10^{-4})$	$^{231}(9\times10^{-4})$					
$3n$	$^{224}(6\times10^{-3})$	$^{225}(7\times10^{-4})$	$^{230}(4\times10^{-4})$					
$4n$	$^{223}(6\times10^{-3})$	$^{224}(1\times10^{-4})$	$^{229}(2\times10^{-4})$					
$5n$	$^{222}(1\times10^{-3})$	$^{223}(9\times10^{-5})$	$^{228}(2\times10^{-5})$					
$6n$	$^{221}(1\times10^{-3})$	$^{222}(2\times10^{-5})$	$^{227}(1\times10^{-5})$					
$7n$	$^{220}(1\times10^{-4})$	$^{221}(1\times10^{-6})$	$^{226}(1\times10^{-7})$					
^{24}Mg+	^{204}Pb	^{209}Bi						
$1n1p$	$^{226}(8\times10^{-7})$	$^{231}(5\times10^{-5})$						
$2n1p$	$^{225}(3\times10^{-4})$	$^{230}(2\times10^{-4})$						
$3n1p$	$^{224}(1\times10^{-4})$	$^{229}(4\times10^{-4})$						
$4n1p$	$^{223}(2\times10^{-4})$	$^{228}(9\times10^{-5})$						
$5n1p$	$^{222}(1\times10^{-4})$	$^{227}(1\times10^{-4})$						
$6n1p$	$^{221}(5\times10^{-5})$	$^{226}(1\times10^{-5})$						
$7n1p$	$^{220}(3\times10^{-7})$	$^{225}(1\times10^{-7})$						
^{24}Mg+	^{209}Bi							
$1n1\alpha$	$^{228}(2\times10^{-5})$							
$2n1\alpha$	$^{227}(5\times10^{-4})$							
$3n1\alpha$	$^{226}(2\times10^{-4})$							
$4n1\alpha$	$^{225}(3\times10^{-4})$							
$5n1\alpha$	$^{224}(2\times10^{-4})$							
$6n1\alpha$	$^{223}(2\times10^{-4})$							
$7n1\alpha$	$^{222}(5\times10^{-6})$							

is broader in the tip-tip collision for the deformed reaction system.

Production cross sections are highly dependent on projectile isotopes in the MNT reactions. The new proton-rich actinides are related to the N/Z ratio of the reaction system. The neutron-deficient nuclides ^{110}Sn and ^{118}Xe induced reactions are favorable for producing heavy neutron-deficient isotopes with the elements of $Z = 95$–100. Furthermore, the ^{94}Rh induced reaction $^{94}\mathrm{Rh} + ^{238}\mathrm{U}$ is better for producing new neutron-deficient Np and Pu. The numerous unknown neutron-deficient nuclei from $Z = 93$ to $Z = 100$ are predicted with the production cross sections via the MNT and FE reactions, which are listed in Tables I, II, and III. The FE reactions are still most promising to synthesize new neutron-deficient actinide nuclei. In addition, the MNT reactions with radioactive beams provide an alternative pathway, which has the advantage of a wide region of new isotopes.

ACKNOWLEDGMENTS

This work was supported by the National Natural Science Foundation of China (Projects No. 11722546 and No. 11675226) and the Talent Program of South China University of Technology.

[1] H. B. Yang, L. Ma, Z. Y. Zhang, C. L. Yang, Z. G. Gan, M. M. Zhang, M. H. Huang, L. Yua, J. Jiang, Y. L. Tian, Y. S. Wang, J. G. Wang, Z. Liu, M. L. Liu, L. M. Duan, S. G. Zhou, Z. Z. Ren, X. H. Zhou, H. S. Xu, and G. Q. Xiao, Alpha decay properties of the semi-magic nucleus ^{219}Np, Phys. Lett. B **777**, 212 (2018).

[2] H. B. Yang, Z. Y. Zhang, J. G. Wang, Z. G. Gan, L. Ma, L. Yu, J. Jiang, Y. L. Tian, B. Ding, S. Guo, Y. S. Wang, T. H. Huang, M. D. Sun, K. L. Wang, S. G. Zhou, Z. Z. Ren, X. H. Zhou, H. S. Xu, and G. Q. Xiao, Alpha decay of the new isotope ^{215}U, Eur. Phys. J. A **51**, 88 (2015).

[3] L. Ma, Z. Y. Zhang, Z. G. Gan, H. B. Yang, L. Yu, J. Jiang, J. G. Wang, Y. L. Tian, Y. S. Wang, S. Guo, B. Ding, Z. Z. Ren, S. G. Zhou, X. H. Zhou, H. S. Xu, and G. Q. Xiao, α-decay properties of the new isotope ^{216}U, Phys. Rev. C **91**, 051302 (2015).

[4] C. A. Laue, K. E. Gregorich, R. Sudowe, M. B. Hendricks, J. L. Adams, M. R. Lane, D. M. Lee, C. A. McGrath, D. A. Shaughnessy, D. A. Strellis, E. R. Sylwester, P. A. Wilk, and D. C. Hoffman, New plutonium isotope: ^{231}Pu, Phys. Rev. C **59**, 3086 (1999).

[5] H. M. Devaraja, S. Heinz, O. Beliuskina, V. Comas, S. Hofmann, C. Hornung, G. Mnzenberg, K. Nishio, D. Ackermann, Y. K. Gambhir, M. Gupta, R. A. Henderson, F. P. Heberger, J. Khuyagbaatar, B. Kindler, B. Lommel, K. J. Moody, J. Maurer, R. Mann, A. G. Popeko, D. A. Shaughnessy, M. A. Stoyer, and A. V. Yeremin, Observation of new neutron-deficient isotopes with Z $\geqslant$ 92 in multinucleon transfer reactions, Phys. Lett. B **748**, 199-203 (2015).

[6] H. Sakurai, Nuclear physics with RI Beam Factory, Front. Phys. **13**, 132111 (2018).

[7] V. Zagrebaev and W. Greiner, Low-energy collisions of heavy nuclei: dynamics of sticking, mass transfer and fusion, J. Phys. G **34**, 1 (2007); New way for the production of heavy neutron-rich nuclei, **35**, 125103 (2008).

[8] V. Zagrebaev and W. Greiner, Synthesis of superheavy nuclei: A search for new production reactions, Phys. Rev. C **78**, 034610 (2008); Production of New Heavy Isotopes in Low-Energy Multinucleon Transfer Reactions, Phys. Rev. Lett. **101**, 122701 (2008).

[9] C. Golabek and C. Simenel, Collision Dynamics of Two ^{238}U Atomic Nuclei, Phys. Rev. Lett. **103**, 042701 (2009).

[10] K. Sekizawa and K. Yabana, Time-dependent Hartree-Fock calculations for multinucleon transfer and quasifission processes in the $^{64}\mathrm{Ni} + ^{238}\mathrm{U}$ reaction, Phys. Rev. C **93**, 054616 (2016).

[11] L. Guo, C. Simenel, L. Shi, and C. Yu, The role of tensor force in heavy-ion fusion dynamics, Phys. Lett. B **782**, 401 (2018).

[12] X. Jiang and N. Wang, Production mechanism of neutron-rich nuclei around N = 126 in the multi-nucleon transfer reaction $^{132}\mathrm{Sn} + ^{208}\mathrm{Pb}$, Chin. Phys. C **42**, 104105 (2018).

[13] A. Winther, Grazing reactions in collisions between heavy nuclei, Nucl. Phys. A **572**, 191 (1994); Dissipation, polarization and fluctuation in grazing heavy-ion collisions and the boundary to the chaotic regime, **594**, 203 (1995).

[14] http://www.to.infn.it/nanni/grazing.

[15] K. Zhao, Z. Li, N. Wang, Y. Zhang, Q. Li, Y. Wang, and X. Wu, Production mechnasim of neutron-rich transuranium nuclei in $^{238}\mathrm{U} + ^{238}\mathrm{U}$, Phys. Rev. C **92**, 024613 (2015).

[16] Z. Q. Feng, G. M. Jin, and J. Q. Li, Production of heavy isotopes in transfer reactions by collisions of $^{238}\mathrm{U} + ^{238}\mathrm{U}$, Phys. Rev. C **80**, 067601 (2009).

[17] G. G. Adamian, N. V. Antonenko, V. V. Sargsyan, and W. Scheid, Possibility of production of neutron-rich Zn and Ge isotopes in multinucleon transfer reactions at low energies, Phys. Rev. C **81**, 024604 (2010); Predicted yields of new neutron-rich isotopes of nuclei with $Z = 64$–80 in the multinucleon transfer reaction $^{48}\mathrm{Ca} + ^{238}\mathrm{U}$, **81**, 057602 (2010).

[18] A. G. Artukh, V. V. Avdeichikov, G. F. Gridnev, V. L. Mikheev, V. V. Volkov, and J. Wilczynski, New isotopes ^{29,30}Mg, ^{31,32,33}Al, ^{33,34,35,36}Si, ^{35,36,37,38}P, ^{39,40}S and ^{41,42}Cl produced in bombardment of a ^{232}Th target with 290 MeV ^{40}Ar ions, Nucl. Phys. A **176**, 284 (1971).

[19] A. G. Artukh, G. F. Gridnev, V. L. Mikheev, V. V. Volkov and J. Wilczynski, Multinucleon transfer reactions in the $^{232}\mathrm{Th} + ^{22}\mathrm{Ne}$ system, Nucl. Phys. A **211**, 299 (1973).

[20] A. G. Artukh, G. F. Gridnev, V. L. Mikheev, V. V. Volkov and J. Wilczynski, Transfer reactions in the interaction of ^{40}Ar with ^{232}Th, Nucl. Phys. A **215**, 91 (1973).

[21] K. D. Hildenbrand, H. Freiesleben, F. Phlhofer, W. F. W. Schneider, R. Bock, D. V. Harrach, and H. J. Specht, Reaction between ^{238}U and^{238}U at 7.42 MeV/Nucleon, Phys. Rev. Lett. **39**, 1065 (1977).

[22] P. Glässel, D. V. Harrach, Y. Civelekoglu, R. Männer, H. J. Specht, J. B. Wilhelmy, H. Freiesleben, and K. D. Hildenbrand, Three-Particle Exclusive Measurements of the Reactions $^{238}\mathrm{U} + ^{238}\mathrm{U}$ and $^{238}\mathrm{U} + ^{248}\mathrm{Cm}$, Phys. Rev. Lett. **43**, 1483 (1979).

[23] K. J. Moody, D. Lee, R. B. Welch, K. E. Gregorich, G. T. Seaborg, R. W. Lougheed, and E. K. Hulet, Actinide production

in reactions of heavy ions with ^{248}Cm, Phys. Rev. C **33**, 1315 (1986).

[24] R. B. Welch, K. J. Moody, K. E. Gregorich, D. Lee, and G. T. Seaborg, Dependence of actinide production on the mass number of the projectile: Xe+^{248}Cm, Phys. Rev. C **35**, 204 (1987).

[25] E. M. Kozulin, E. Vardaci, G. N. Knyazheva, A. A. Bogachev, S. N. Dmitriev, I. M. Itkis, M. G. Itkis, A. G. Knyazev, T. A. Loktev, K. V. Novikov, E. A. Razinkov, O. V. Rudakov, S. V. Smirnov, W. Trzaska, and V. I. Zagrebaev, Mass distributions of the system ^{136}Xe + ^{208}Pb at laboratory energies around the Coulomb barrier: A candidate reaction for the production of neutron-rich nuclei at $N = 126$, Phys. Rev. C **86**, 044611 (2012).

[26] J. S. Barrett, W. Loveland, R. Yanez *et al.*, ^{136}Xe + ^{208}Pb reaction: A test of models of multinucleon transfer reactions, Phys. Rev. C **91**, 064615 (2015).

[27] Y. X. Watanabe *et al.*, Pathway for the Production of Neutron-Rich Isotopes around the $N = 126$ Shell Closure, Phys. Rev. Lett. **115**, 172503 (2015).

[28] E. M. Kozulin, V. I. Zagrebaev, G. N. Knyazheva, I. M. Itkis, K. V. Novikov, M. G. Itkis, S. N. Dmitriev, I. M. Harca, A. E. Bondarchenko, A. V. Karpov, M. G. Itkis, S. N. Dmitriev, I. M. Harca, A. E. Bondarchenko, A. V. Karpov, V. V. Saiko, and E. Vardaci, Inverse quasifission in the reactions ^{156,160}Gd + ^{186}W, Phys. Rev. C **96**, 064621 (2017).

[29] S. Wuenschel, K. Hagel, M. Barbui, J. Gauthier, X. G. Cao, R. Wada, E. J. Kim, Z. Majka, R. Planeta, Z. Sosin, A. Wieloch, K. Zelga, S. Kowalski, K. Schmidt, C. Ma, G. Zhang, and J. B. Natowitz, Experimental survey of the production of α-decaying heavy elements in ^{238}U + ^{232}Th reactions at 7.5–6.1 MeV/nucleon, Phys. Rev. C **97**, 064602 (2018).

[30] C. H. Dasso, G. Pollaro, and A. Winther, Systematics of Isotope Production with Radioactive Beams, Phys. Rev. Lett. **73**, 1907 (1994); Particle evaporation following multinucleon transfer process with radioactive beams, Phys. Rev. C **52**, 2264 (1995).

[31] L. W. David, The synthesis of new neutron-rich heavy nuclei, Front. Phys. **7**, 23 (2019).

[32] V. V. Volkov, Deep inelastic transfer reactions — The new type of reactions between complex nuclei, Phys. Rep. **44**, 93 (1978).

[33] G. G. Adamian, N. V. Antonenko, W. Scheid *et al.*, Treatment of competition between complete fusion and quasifission in collisions of heavy nuclei, Nucl. Phys. A **627**, 361 (1997).

[34] G. G. Adamian, N. V. Antonenko, W. Scheid *et al.*, Fusion cross sections for superheavy nuclei in the dinuclear system concept, Nucl. Phys. A **633**, 409 (1998).

[35] W. Li, N. Wang, J. F. Li *et al.*, Fusion probability in heavy-ion collisions by a dinuclear-system model, Europhys. Lett. **64**, 750 (2003).

[36] Z. Q. Feng, G. M. Jin, F. Fu *et al.*, Entrance channel dependence of production cross sections of superheavy nuclei in cold fusion reactions, Chin. Phys. Lett. **22**, 846 (2005).

[37] Z. Q. Feng, G. M. Jin, F. Fu, and J. Q. Li, Production cross sections of superheavy nuclei based on dinuclear system model, Nucl. Phys. A **771**, 50 (2006); Z. Q. Feng, G. M. Jin, J. Q. Li, and W. Scheid, Formation of superheavy nuclei in cold fusion reactions, Phys. Rev. C **76**, 044606 (2007).

[38] Z. Q. Feng, G. M. Jin, and J. Q. Li, Production of new superheavy $Z = 108$–114 nuclei with ^{238}U, ^{244}Pu, and ^{248,250}Cm targets, Phys. Rev. C **80**, 057601 (2009); Z. Q. Feng, G. M. Jin, J. Q. Li, and W. Scheid, Production of heavy and superheavy nuclei in massive fusion reactions, Nucl. Phys. A **816**, 33 (2009).

[39] Z. Q. Feng, G. M. Jin, and J. Q. Li, Influence of entrance channels on the formation of superheavy nuclei in massive fusion reactions, Nucl. Phys. A **836**, 82 (2010).

[40] J. Q. Li and G. Wolschin, Distribution of the dissipated angular momentum in heavy-ion collisions, Phys. Rev. C **27**, 590 (1983).

[41] W. Nörenberg, Quantum-statistical approach to gross properties of peripheral collisions between heavy nuclei, Z. Phys. A **274**, 241 (1975).

[42] G. Wolschin and W. Nörenberg, Analysis of relaxation phenomena in heavy-ion collisions, Z. Phys. A **284**, 209 (1978).

[43] P. H. Chen, Z. Q. Feng, J. Q. Li, and H. F. Zhang, Production of proton-rich nuclei around Z = 84-90 in fusion-evaporation reactions, Eur. Phys. J. A **53**, 95 (2017).

[44] V. Yu. Denisov and W. Nörenberg, Entrance channel potentials in the synthesis of the heaviest nuclei, Eur. Phys. J. A **15**, 375 (2002).

[45] Z. Q. Feng, G. M. Jin, F. Fu, and J. Q. Li, Isotopic dependence of production cross sections of superheavy nuclei in hot fusion reactions, Chin. Phys. C **31**, 366 (2007).

[46] P. H. Chen, Z. Q. Feng, J. Q. Li, and H. F. Zhang, A statistical approach to describe highly excited heavy and superheavy nuclei, Chin. Phys. C **40**, 091002 (2016).

[47] X. J. Bao, Possibility to produce ^{293,295,296}Og in the reactions ^{48}Ca + ^{249,250,251}Cf, Phys. Rev. C **100**, 011601(R) (2019).

[48] X. J. Bao, S. Q. Guo, H. F. Zhang, and J. Q. Li, Dynamics of complete and incomplete fusion in heavy ion collisions, Phys. Rev. C **97**, 024617 (2018).

[49] S. Q. Guo, Y. Gao, J. Q. Li, and H. F. Zhang, Dynamical deformation in heavy ion reactions and the characteristics of quasifission products, Phys. Rev. C **96**, 044622 (2017).

[50] J. V. Kratz, M. Schädel, and H. W. Gäggeler, Reexamining the heavy-ion reactions ^{238}U + ^{238}U and ^{238}U + ^{248}Cm and actinide production close to the barrier, Phys. Rev. C **88**, 054615 (2013).

[51] P. H. Chen, F. Niu, Y. F. Guo, and Z. Q. Feng, Nuclear dynamics in multinucleon transfer reactions near Coulomb barrier energies, Nucl. Sci. Technol. **29**, 185 (2018).

[52] P.-H. Chen, F. Niu, W. Zuo, and Z.-Q. Feng, Approaching the neutron-rich heavy and superheavy nuclei by multinucleon transfer reactions with radioactive isotopes, Phys. Rev. C **101**, 024610 (2020).

[53] Z.-Q. Feng, Production of neutron-rich isotopes around $N = 126$ in multinucleon transfer reactions, Phys. Rev. C **95**, 024615 (2017).

[54] G. M. Jin, Y. X. Xie, Y. T. Zhu *et al.*, Product cross sections for the reaction of ^{12}C with ^{209}Bi, Nucl. Phys. A **349**, 285 (1980).

[55] M. Wang, G. Audi, F. G. Kondev, W. J. Huang, S. Naimi, and X. Xu, The AME2016 atomic mass evaluation (II). Tables, graphs and references, Chin. Phys. C **41**, 030003 (2017).